The SkyHopper Space Telescope Earthshine & Zodiacal Light Science Requirements

By

Sarah Elizabeth Caddy

A thesis submitted to Macquarie University
for the degree of Master of Research
Department of Physics and Astronomy
October 2019

MACQUARIE
University
SYDNEY·AUSTRALIA

Typeset in LaTeX 2_ε.

Except where acknowledged in the customary manner, the material presented in this thesis is, to the best of my knowledge, original and has not been submitted in whole or part for a degree in any university.

Sarah Elizabeth Caddy

Acknowledgements

I'd like to thank the SkyHopper consortium for their support of this work and for allowing me to collaborate on this project. It has been such an enriching experience and I can't wait to see what awaits SkyHopper in the future.

Lots of thanks to the Huntsman Telescope team, Dr Anthony Horton, Wilfred Gee, Amir Ebadati Bazkiaei, Jaime Andres Alvarado Montes and Fergus Longbottom for their amazing support.

A big thank you to my partner for always being a shoulder to lean on and a mind to bounce ideas from.

I'd like to thank my Dad, Mum and brother for their endless love. I wouldn't be looking to the stars today without your support.

And last but not least, I'd like to thank my teacher and supervisor Dr Lee Spitler whose passion and enthusiasm to explore the Universe inspires me every day. Thank you for your patience and for your guidance.

Abstract

The SkyHopper Space Telescope is an ambitious new facility that is on target to become Australia's first satellite based space telescope. One key science goal of the SkyHopper mission is to make an accurate measurement of the Cosmic Optical and Infrared Background (COIB). Primordial galaxies from the epoch of reionization are sources that are currently thought to contribute to the COIB. However, the existing conflict between photometric measurements and lower limits from integrated galaxy counts suggest that there may be a diffuse emission largely undetected due to the lack of control of systematic errors. Achieving an accurate measurement of the COIB will help to improve our understanding the origin of the sources that re-ionized the universe. Critical to the success of detecting the COIB with SkyHopper is systematic error control. In this thesis I address this by presenting a new method for correlating the Earthshine detected by a space telescope with NASA CERES satellite weather data. I construct a Bayesian optical payload instrument model from which I identify science requirements for the SkyHopper telescope design. This thesis works focuses on the need to successfully measure Zodiacal light strength, which is the most challenging aspect of measuring the COIB.

Contents

List of Figures

List of Tables

" Take chances, make mistakes, get messy. "

Ms Kim Delaney: My high school physics & chemistry teacher

1 Introduction

Can a small, shoebox-sized satellite make an accurate measurement of the light from the first galaxies that existed in our universe? This is the question we hope to answer with SkyHopper, Australia's first satellite based space telescope.

The SkyHopper Space Telescope is a project in development by a consortium of collaborating universities in Australia and overseas. Funding for the first stages of preliminary design and development has been secured [Trenti, 2018a] and a large infrastructure grant is currently under assessment. The SkyHopper team aim to pave the way for Australia's entrance into space-based astronomical observations.

Space telescopes have revolutionised our understanding of our place in the Universe. Conducting astronomical observations from space allows access to wavelengths otherwise absorbed by the atmosphere, providing sharp, lower noise images than ground-based telescopes [Trenti, 2018a] and in some cases continuous access to the sky.

Arguably the most successful and well known of these space telescopes is the Hubble Space Telescope. Since its launch in 1990, Hubble has lead the search for the first galaxies that existed in the Universe [Trenti et al., 2011], to the discovery of the accelerating expansion of the Universe through observations of distant supernovae winning the Nobel prize in 2011 [Schmidt, 2012].

But all of this comes at a significant price: the costs associated with designing, building, operating and servicing Hubble with the Space Shuttle program is estimated to have reached US $10 billion dollars in 2010 [Ballhaus et al., 2010]. Hubble's successor the James Webb Space Telescope (JWST), despite having started development over 20 years ago by three of the worlds leading space agencies NASA, ESA and Canada, Webb faces more launch delays. The current launch target of March 2021 has been a long time coming, with significant delays due to integration and testing issues with a total projected price tag of US $8.835 billion for a 7 year mission [Gardner et al., 2006].

The question is then: how do we build inexpensive, low risk space telescopes that are still agile, responsive, robust and resilient? One solution is to make them smaller.

The miniaturisation of satellites has come a long way since the launch of Hubble. Hundreds of cube satellites are now being delivered to orbit weighing no more than 1 to $20kg$ [Trenti, 2018a]. There has been a growing focus on producing custom designed, low cost spacecraft busses that can be delivered to orbit with specialised instrumentation in commercial rockets. At a crucial point in Australia's entrance into space science with the recent the

Figure 1.1: SkyHopper's logo is a Spinifex Hopping mouse. A small, fast and nimble Australian native. These are all qualities the SkyHopper Space Telescope aims to embody.

launch of the Australian Space Agency, the SkyHopper team will push the boundaries of the science capable of a cube satellite, and will aim to uncover the light from the first galaxies in our Universe.

1.1 Motivation

Developing the initial science requirements for the SkyHopper COIB project is the focus of this thesis. SkyHopper is being designed to measure a fundamental phenomenon in observational cosmology known as Cosmic Optical and Infrared Background (COIB) radiation, which is the sum of light from all unresolved sources that are too faint to detect directly over the wavelength ranges of $0.3 - 300\mu m$ [Hill et al., 2018].

The epoch of reionization marks a period in the Universe's history where the ultraviolet emissions from the first stars in the Universe began to ionize the intergalactic medium [Zemcov et al., 2011]. This is a process which is thought to be underway by redshift $z \geq 10$ and completed by $z \sim 5$ [Zemcov et al., 2011]. This set the initial conditions for the subsequent structure formation in the Universe. Galaxies in the epoch of reionization are known to contribute to the COIB signal [Zemcov et al., 2011] via the processes of stellar emissions from nucleosythesis [Hauser and Dwek, 2001], however measurements of the COIB to date lack the control of systematic errors required to constrain the COIB to within an order of magnitude [Zemcov et al., 2013].

Estimates of the COIB have historically been of two methods: integrated galaxy counts and direct measurements [Bethermin, 2011]. The inconsistencies that have arisen from the results of these two methods have raised a number of open questions that the SkyHopper team aim to explore.

The search for light from the most distant galaxies continues to be an active area of research today [Robertson et al., 2015]. Extrapolating the total light from galaxy count surveys provides a lower limit on the expected emission from these galaxies and currently they account for an estimated 75% of the light [Hauser and Dwek, 2001]. Upper limits from attempted direct measurement complicate this, with estimates observed at over five times that which is derived from more recent work using galaxy counts [Driver et al., 2016]. The conflict between absolute photometric measurements of the COIB and estimates from the summed contributions of detected galaxies indicates that there may be a diffuse emission detectable with the right instrument, and aggressive systematic error control [Zemcov et al.,

2013].

Deep pencil beam surveys [Bouwens et al., 2009] and current pure parallel surveys such as BoRG [Trenti et al., 2011] are now locating the brightest of the reionizing galaxies in the epoch of reionization. There may be many more fainter sources undetected and as a result Zemcov et al. [2013] states: "the Universe was re-ionized by many faint sources rather than few bright ones".

The process of structure formation in the Universe at the time of the epoch of reionization to the present is traced by the COIB [Hauser and Dwek, 2001]. The spectral energy distribution (SED) of the light from this epoch provides constraints of stellar formation [Zemcov et al., 2017], active galactic nuclei activity and dust properties [Driver et al., 2016] which has been described by Zemcov et al. [2017] as the "benchmark against which to judge theories of structure formation."

Further insight into how and when reionization occurred and its transformation of the Universe are important steps toward insight into structure formation [Gardner et al., 2006].

1.2 Challenges

Measurement of the COIB is both a technical and astrophysical challenge [Korngut et al., 2013]. Current direct measurements of the COIB are largely inconsistent with one another (see figure 1.2) due to the broad methods of foreground removal used to isolate the COIB from bright foreground sources [Cooray, 2016, Zemcov et al., 2017]. The SED of the COIB is expected to be relatively featureless, and thus has no single spectral signature as it depends upon a complex mixture of sources throughout cosmic time [Hauser and Dwek, 2001, Hill et al., 2018, Mattila and Väisänen, 2019, Driver et al., 2016]. Due to the strength of the isotropic signal from the COIB, subtraction and accurate modelling of foreground sources remains one of the most challenging obstacles that continues to make measurement of the COIB difficult.

1.2.1 Earthshine Foreground Emission

Light that is reflected and emitted from the Earths surface is known as Earthshine. This encompasses both longwave outgoing radiation between $5 - 200\mu m$ characterized by the Earth's thermal emission from the surface and atmosphere from absorbed solar radiation, and shortwave outgoing radiation between $0.3 - 5\mu m$ characterized by a scattered solar spectrum with the addition of absorption features from the atmosphere and surface features such as forests, oceans and deserts [Giavalisco, 2002].

Little work has been done to understand the impact of Earthshine on low Earth orbiting space telescopes. The easiest solution is to simply avoid it by restricting the telescope limb angle, Sun angle, and Sun altitude [Giavalisco et al., 2002]. Studies into the background observed by Hubble have been performed by the Space Telescope Science Institute (STScI) in order to understand the contribution of Earthshine to observed background for the Advanced Camera for Surveys (ACS) at small Earth limb angles [Biretta et al., 2003, Giavalisco et al., 2002]. At visible to near infrared wavelengths the primary contributor to Earthshine is found to be incident solar radiation reflected by the atmosphere and surface as well as residual air glow. At these wavelengths, Earthshine is mostly independent of the underlying surface due to the optical depth of the atmosphere [Cox et al. 1987].

These wavelengths pose significant challenges to space based optical and infrared telescopes due to randomly varying cloud coverage, and so can not be modeled with a simple modified solar spectrum as discussed by Giavalisco et al. [2002]. This issue is addressed

by estimating Earthshine contributions in low, average, high and very high Earthshine background however it is stressed by STScI that these may not reflect true conditions during operation [Giavalisco et al., 2002]. As a result it is important to gain an in-depth understanding of the contribution of Earthshine to the background detected in space telescope images, and derive constraints to avoid it if possible.

1.2.2 Zodiacal Light Foreground Emission

Zodiacal light is the dominant source of foreground emission in low Earth orbit and is the main source of error for infrared direct photometric measurements of the COIB [Bethermin, 2011]. Interplanetary dust most densely populating the ecliptic plane scatters Sunlight in both the optical and near-infrared and emits thermal radiation in the mid-infrared to the far-infrared [Korngut et al., 2013]. This dust originates predominately from comets and asteroids, with a small contribution possible from interstellar origins [Krick et al., 2012]. The physical components of this cloud mainly consist of a fairly uniform distribution of dust within the ecliptic plane, with the exception of clumping and a few gaps due to gravitational interaction. Due to our vantage point here on Earth surrounded by this dust in the Solar System, Zodiacal light becomes an unavoidable issue.

Current models of the Zodiacal cloud are based upon observations by the Cosmic Background Explorer Diffuse Infrared Background Experiment (DIRBE with COBE) from $1-240\mu m$ as well as the Infrared Astronomical Satellite (IRAS) observations from $12-100\mu m$ [Krick et al., 2012]. Generally, the SED in the optical to near-infrared portion of the spectrum that SkyHopper will detect is characterized by a reddened solar spectrum with spectral absorption features analogous to that of the Sun [Korngut et al., 2013].

Modelling Zodiacal light alone does not achieve the level of precision required for COIB measurements. For example, the Exposure Time Calculator (ETC) used for signal-to-noise (SNR here after) calculations for Hubble proposals uses models to first order approximation of Zodiacal light surface brightness [Diaz, 2015]. The surface brightness of Zodiacal light depends upon the time of year, direction of observation and, due to its anisotropy, location within the cloud itself. A solution is to exploit the well known SED spectral features of Zodiacal light to make direct measurements of its brightness for subtraction.

1.2.3 Galactic Foreground Emission

Galactic foreground emission is a diffuse optical background produced by the scattering of radiation by dust known as galactic cirrus. The component which is absorbed is remitted in the infrared [Bernstein et al., 2002] and can be seen as the main component of background radiation from low Earth orbit after the removal of Earthshine and Zodiacal light. Due to the observers location within the Galaxy, galactic foreground emission cannot be avoided. The emission will not be addressed in this work and will be the subject of future work, however galactic cirrus is reported to be accurately constrained by current HI data [Bethermin, 2011].

The three methods used by research groups in the past that attempt to navigate the issue of foreground emissions are:

- Eliminating or minimizing foreground emissions by making observations outside of the Earth's atmosphere, or even outside of the Solar System.
- Making use of the spatial variability of foreground features with respect to the isotropic signal from the COIB
- Utilizing the difference in spectral features of foreground emissions with the uniform SED of the COIB

1.2.3.1 COBE and DIRBE

Data from COBE provided the first tentative upper limits using DIRBE data for the direct measurements of a COIB emission reported in 1996 [Hauser and Dwek, 2001, Puget et al., 1996]. Zodiacal light was modeled and subtracting using the Far Infrared Absolute Spectrophotometer data. Over the DIRBE wavelengths of $400\mu m$, significant uncertainty was found due to galactic foreground components mimicking the COIB. The final intensity was reported at $3.4nWm^{-2}sr^{-1}$ in the 400 to $1000\mu m$ range [Puget et al., 1996].

1.2.3.2 Pioneer 10 and 11

Measurements from the Pioneer 10 and 11 missions taken from 1972 to 1974 passed beyond the asteroid belt to a distance greater than 3AU where the Zodiacal component of foreground emission dropped to insignificantly small values [Matsuoka et al., 2011, Mattila and Väisänen, 2019, Hauser and Dwek, 2001] with remaining components of integrated starlight, diffuse galactic light and the COIB. These results were limited due to unavoidable starlight contributions in the large field of view of the photometer [Hauser and Dwek, 2001] which dominates over the far fainter COIB signal. This data was later reanalyzed with a detection of the COIB at 440nm and 640nm presented by Matsuoka et al of $\lambda I_{COIB} = 7.9 \pm 4.0nWm^{-2}sr^{-1}$ and $7.7 \pm 5.8nWm^{-2}sr^{-1}$ respectively [Matsuoka et al., 2011]. This result remains tentative due to the COIB being the difference between two larger quantities: the total sky brightness in the large field of view of the instrument and the total starlight from all faint stars in the field that could not be accounted for [Mattila and Väisänen, 2019].

1.2.3.3 New Horizons

The Long Range Reconnaissance Imager instrument aboard the New Horizons mission was not hindered by the issues faced by Pioneer 10 and 11. The instruments on New Horizons had excellent spatial resolution, which meant that sky background intensities could be isolated from starlight. COIB measurements were obtained with virtually no Zodiacal contamination at 7-17 AU past the orbit of Jupiter in the broadband from $440 - 870nm$ reporting a value of $29.6nWm^{-2}sr-1$ [Zemcov et al., 2017, Mattila and Väisänen, 2019] as an upper limit to COIB intensity. Here, the limiting factor remains diffuse galactic light intensity which could only be addressed via modelling which introduced substantial uncertainties [Mattila and Väisänen, 2019].

1.2.3.4 Very Large Telescope

It is also possible to make use of foreground features such as dark clouds in order to make differential measurements, avoiding the need for modelling the foreground contributions of Earthhsine, Zodiacal light, galactic diffuse light and the contribution of foreground stars in the galaxy. The method has been attempted multiple times reported in both [Mattila, 1976, 1990] as well as [Boughn and Kuhn, 1986] and [Spinrad and Stone, 1978]. More recent measurements by Mattila et al. [2017] using the European Southern Observatory (ESO) Very Large Telescope (VLT) and spectrophotometry from the Focal Reducer and low dispersion Spectrograph (FORS) of the surface brightness towards the high galactic latitude dark cloud Lynds 1642 produced promising results with a detection of the COIB at $400nm$ of $11.6^{+}_{-}4.4nWm^{-2}sr^{-1}$ [Mattila et al., 2017]. The presence of scattered starlight in the results in the line of sight of the dark cloud result in these measurements being treated as upper limits [Mattila and Väisänen, 2019].

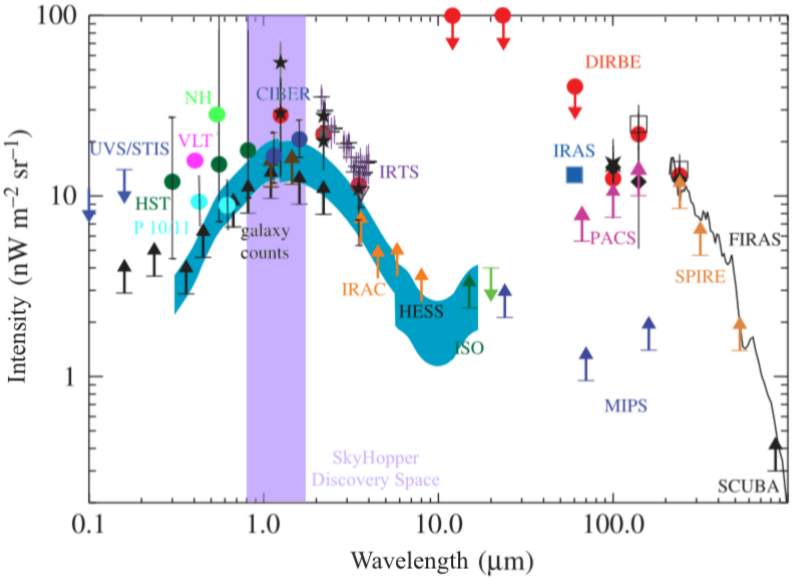

Figure 1.2: The current estimate of the SED of the COIB from independent measurements. SkyHoppers discovery space is highlighted in purple from $0.8 - 1.7\mu m$. For a detailed description of each observation in this graph not described in this thesis please see Cooray [2016]. This figure has been taken and adapted from Cooray's work.

1.2.3.5 Hubble Space Telescope

The dark cloud method relies heavily on the prediction that the SED for the COIB is relatively featureless and smooth, as well as isotropic in distribution about the sky. Utilizing the difference in spectral features of foreground emissions with the uniform SED of the COIB is used as a direct detection method. SED fitting of modeled foreground sources calibrated using direct measurement of the characteristic spectral features of these components allows for detection of the COIB not restricted to the proximity of dark clouds. While being one of the most widely used methods for direct COIB detection it also bares significant uncertainties, as it requires real time measurement of Zodiacal light using characteristic Fraunhofer spectral lines.

Measurement of the COIB with Hubble were pioneered by Bernstein [2007] with the Wide Field Planetary Camera 2 (WFPC2). Bernstein [2007] made use of the relative strength of solar Fraunhofer lines in Zodiacal compared to the solar spectrum in order to make real time measurements of Zodiacal light foreground and subtract it. Critically this program observed the same field simultaneously with the du Pont 2.5 m Telescope at the Las Campanas Observatory to constrain Zodiacal light levels. This effort was complicated by atmospheric air glow emission as well as systematic uncertainties from atmospheric scattering, ground scattering and stray light [Mattila, 2003]. Bernstein [2007] reported a COIB of $12nWm^2sr^{-1}$ at $814nm$.

1.2.3.6 CIBER

Direct Zodiacal light measurement was also conducted using the sounding rocket CIBER (the Cosmic Infrared Background ExpeRiment). For this CIBER also attempted a direct detection of the Zodiacal light intensity in real time with a narrowband spectrometer [Korngut et al., 2013]. CIBER's results point towards significant unaccounted for components of the COIB at $0.8 - 1.7\mu m$ wavelengths [Matsuura et al., 2017]. They report a COIB brightness of

$42.7^{+11.9}_{-10.6} nWm^2sr^1$ at $1.4\mu m$ Matsuura et al. [2017]. However the limited exposure time of a sounding rocket program made the measurement uncertain [Horton et al., 2016]. SkyHopper aims to build upon the methods developed by the CIBER team, and implement them in a long duration program to ensure a secure measurement of both Zodiacal intensity and the COIB.

1.3 Our Solution

Despite the many attempts to measure the COIB directly, results from deep galaxy counts and direct detection still do not converge. Not only this, but reported direct detection values of the COIB from multiple independent studies are inconsistent due to the challenges of foreground emission and systematic errors. If the COIB is directly derived from galaxies, then results from galaxies counts and direct measurement should converge - and this is not yet the case. Absolute measurements of the strength of the background with SkyHopper using accurate foreground modelling and subtraction coupled with thorough systematic error constraints may contribute to a solution.

To provide a conclusive direct measurement of the COIB with SkyHopper (1) all foreground sources of light must be accounted for or avoided completely and (2) a detailed plan must be put in place to constrain and quantify all systematic errors. In this thesis, I explore SkyHoppers ability to meet these challenges by:

1. Developing a novel method of quantifying Earthshine beneath a space telescope in order to derive pointing constraints to avoid it

2. Designing an observing program with SkyHopper to accurately detect and subtract the Zodiacal light foreground emission

3. Constructing an Bayesian instrument model to simulate the performance of the instrument and produce initial systematic error analysis

2

Mission Design and Science Methodology

The design phase of SkyHopper requires a set of specific science requirements to achieve COIB science case goals. In this chapter, I present the overall COIB methodology and mission design which is based upon the CIBER mission.

2.1 SkyHopper Mission Design

The SkyHopper COIB project aspirational goal is to make a 1% measurement of the COIB. The SkyHopper COIB science case is being led by Dr. Lee Spitler in close collaboration with the SkyHopper optical payload Instrument Scientist, Dr. Anthony Horton, and the SkyHopper consortium. The design of the science case comes from the successful CIBER missions (see Bock et al. [2006], Korngut et al. [2013], Tsumura et al. [2010], Matsuura et al. [2017] for a few examples), and an earlier CubeSat space telescope concept known as the Australian Space Eye [Horton et al., 2016]. Details of the optical payload will be discussed below in section 2.2.

SkyHopper's nominal orbit will be a Dawn-Dusk Sun-synchronous in order to maximise power output of its solar panels. At an altitude above the Earth of 500km, the expected duty cycle per orbit is estimated to be 40%. This factors in down-link and up-link requirements and science field pointing constraints to achieve the science goals.

During SkyHopper's $\sim$ 90 minute orbit, $\sim$ 36 minutes will be dedicated to science observations. To facilitate photometric calibration, SkyHopper will take a short exposure for determination of the magnitude of bright foreground sources in a science field (defined in section 4.1). For the main science observations, SkyHopper will image simultaneously with 4 broadband filters (covering the optical/near-infrared) and 2 narrowband filters (for Zodiacal measurement) with a custom designed Kesters prism (see Figure 2.1). This will enable a simultaneous imaging of the COIB and characterisation of the Zodiacal light foreground.

Baffling on the instrument is used to restrict stray light from entering the telescope aperture. This will be deployable after launch to meet the space requirements for the commercial deployment of cube satellites that occupy standard sizes. As a result, deployable baffling about the aperture of the telescope presents a significant risk to the mission, as does all moving parts. In order to reduce this risk, the baffle while stored un-deployed must not cover the aperture of the telescope, in the event that deployment fails. This ensure the success of de-scoped missions that do not require strict stray light minimisation. To reduce the impact of stray light from the surface of the Earth, orbital restriction will be derived in chapter 3.

The telescope will not be fitted with a shutter, as any moving part placed in front of the aperture presents significant risk in the event of failure, and so dark calibration frames and flats cannot be taken. To mitigate this, the detector will be fitted with calibration reference pixels, but spatial variation across the detector is still expected. This will be modeled in chapter 4, using a Bayesian instrument model.

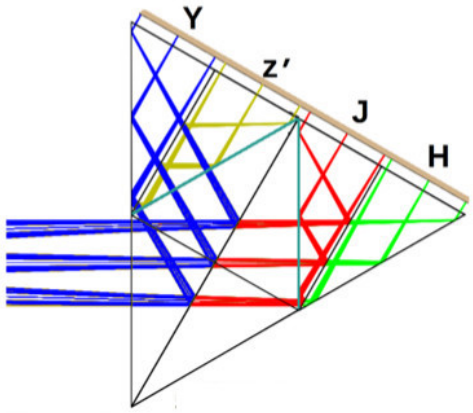

Figure 2.1: The Kesters prism design mounted on the Hawaii-2RG detector. Each filter bandpass will arrange on the detector resulting in three 2048×512 pixel segments for Y, J and H band, with the ON and OFF narrowbands located as 682×512 pixel segments in the Z' band. This novel design will enable simultaneous multi-band imaging and is the first to be utilised in a cube satellite [Trenti, 2018b].

The COIB science requirements will be considered along side with requirements from two other science missions. The first aims to identify Earth-sized exoplanets around ultra cool, low mass dwarf stars. The second is the rapid followup of gamma-ray bursts in order to quickly identify high-redshift ($z > 6$) gamma-ray burst candidates.

2.2 Optical Payload

The spacecraft bus will be provided by the American satellite company Blue Canyon Technologies. The $200 \times 100mm$ 12-unit CubeSat bus will house the optical payload: a reflecting telescope described below. The payload will include a Hawaii-2RG infrared detector, the same detector used on JWST [Finger et al., 2004]. The detector will be actively cooled to $\sim 140K$ using cryocooler technology.

2.2.1 Optics

The SkyHopper science payload design includes a rectangular entrance aperture of $200mm \times 100mm$. A primary baffle will minimise stray light from the Sun, Moon and Earth. The telescope will have 4 arcsecond per pixel sampling and will be constructed using a series of 4 aluminium reflecting surfaces forming a compound reflecting telescope design, within the spacecraft bus total length on each optical axis.

2.2.2 Detector

The Hawaii-2RG Teledyne imaging sensor is a research grade, visible to infrared detector optimized for space telescope operations (see [Teledyne] for details). The detector itself has an array of 2048×2048 pixels, with pixel size of $18\mu m$ of which the detector will be split into 4 subsections for each filter bandpass enabling simultaneous imaging in all 4 bands and are arranged in 2048×512 pixels on the detector for Y J and H bands. The two narrow bandpasses will be placed over the z' filter, each with 512×682. The dark current, read noise and quantum efficiency of the detector over the wavelength range can be found in A.2.

The Hawaii-2RG has already undergone significant testing both in a lab based environment and in the field and is proven to uphold the high operating standards quoted by Teledyne [Loose

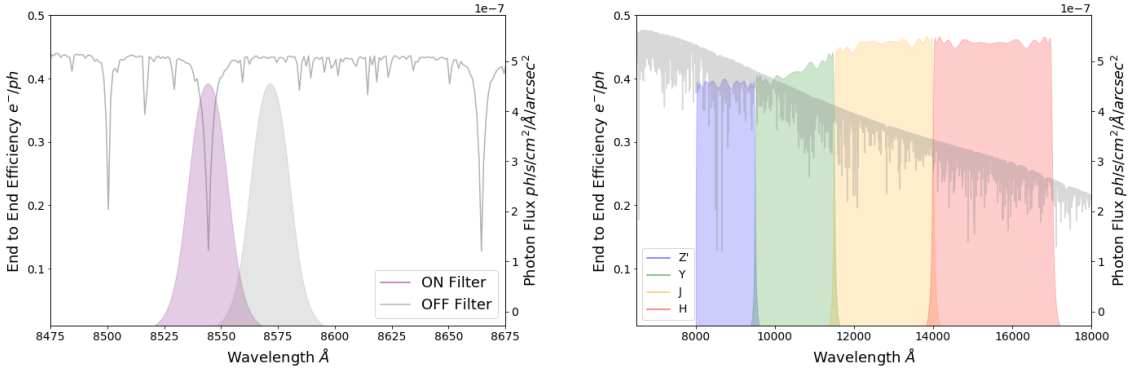

Figure 2.2: *Left:* SkyHopper narrowband filter design. The ON filter is centered on the strongest calcium triplet absorption feature in Zodiacal light. The OFF filter will measure the adjacent continuum. The different in the flux from these two filters will result in a background subtracted measurement of the line flux at 8542Angstrom. *Right:* SkyHopper broadband filter design. These filters will be used to measure the COIB.

et al., 2010, Rauscher et al., 2011].

2.3 Science Methodology for Zodiacal Light Detection

Direct measurement of Solar Fraunhofer lines in Zodiacal light emission is a proven method for Zodiacal light detection and subtraction [Korngut et al., 2013, Tsumura et al., 2010, Zemcov et al., 2013]. The equivalent width of Solar Fraunhofer lines in the Zodiacal light spectrum has been shown to match that of the Solar spectrum, with a width of $0.37nm$ [Korngut et al., 2013]. The calcium II triplet lines at $849.8nm$, $854.2nm$ and $866.2nm$ are one of the strongest absorption features in the Zodiacal light spectrum, and the strongest of these lines at $854.2nm$ will be used to directly detect the relative strength of the Zodiacal light foreground.

Following the design of CIBER, SkyHopper will also have 2 narrow band filters (ON and OFF) in the z' band which I choose to be centered on $854.2nm$ and $857.2nm$ respectively in order to measure the strength of a strong absorption feature in the Zodiacal light, the calcium triplet feature at $854.2nm$ and the absolute sky brightness of the nearby continuum. I choose $857.2nm$ to ensure that the extrapolated continuum (if there were no absorption feature) is the same as the nearby continuum, with no contaminating absorption features.

The photocurrent detected by the off band narrow-band filter will be given by:

$$i_{off} = \frac{\eta\Omega}{hc}\int I(\lambda)^{cont}_{ZL}T(\lambda) - I(\lambda)^{line}_{ZL} + I(\lambda)_{COIB}T(\lambda) \tag{2.1}$$

Where η is the peak efficiency, h and c are Planks constant and the speed of light respectively and $T(\lambda)$ is the instrument response function. $I(\lambda)^{cont}_{ZL}$ is the Zodiacal light continuum surface brightness, $I(\lambda)^{line}_{ZL}$ is the Zodiacal light line strength and $I(\lambda)_{COIB}$ is the COIB continuum surface brightness. Similarly for the on band narrow-band filter we have:

$$i_{on} = \frac{\eta\Omega}{hc}\int I(\lambda)^{cont}_{ZL}T(\lambda) + I(\lambda)_{COIB}T(\lambda) \tag{2.2}$$

We now use the definition of the equivalent width of the line W:

$$I(\lambda)^{line}_{ZL} = I(\lambda)^{cont}_{ZL}W \tag{2.3}$$

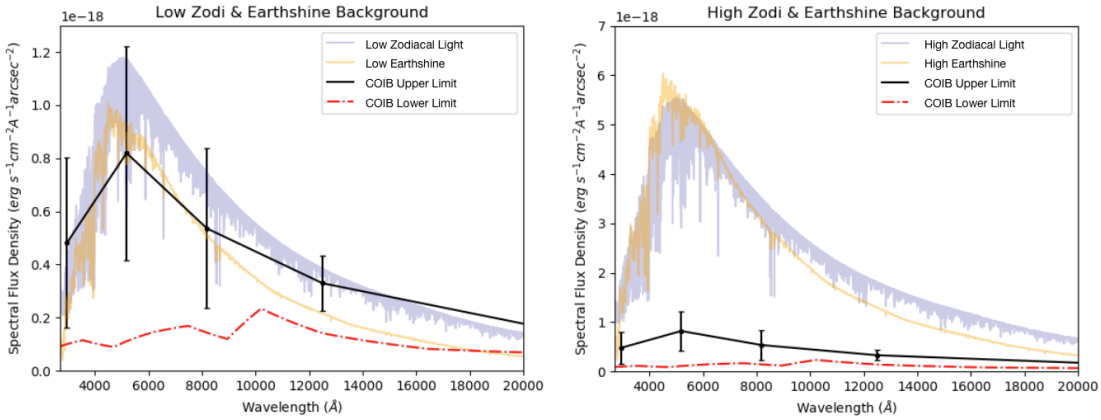

Figure 2.3: The upper and lower limits for the Zodiacal light SED, Earthshine SED (top of the atmosphere) and estimates of the COIB SED used in this work and presented in Table A.1.

To derive:

$$i_{off} - i_{on} = \frac{\eta\Omega}{hc} I(\lambda)^{cont}_{ZL} W \tag{2.4}$$

Which is used to isolate the continuum strength at the line. This can then be used to normalise the well characterised Zodiacal light spectrum to the observed intensity for accurate foreground subtraction. The normalised Zodiacal light spectrum used in this work for upper and lower limits as well as COIB and Earthshine upper and lower limits given in Table A.1 are shown for reference in Figure 2.3.

SkyHopper will also be equipped with both broadband filters for simultaneous imaging in the z', J, H, and K bands from $0.8 - 1.7\mu m$. This will enable broadband imaging of the COIB and Zodiacal light SED.

3

Predicting Earthshine

In order to understand the impact of the strength and variability of Earthshine on the SkyHopper mission, I correlate sky background estimates from archival Hubble Space Telescope data, with the upwards flux from the top of the atmosphere *"Earthshine"* monitored by NASA weather satellites. For this study I construct a python package that is currently in development and is used to calculate the Earthshine present below any low Earth orbit optical system. Below I present the results of this study and use them to derive SkyHoppers pointing requirements. I also present supporting evidence for the impact of Zodiacal light on space based observations, which emerge in the Hubble sky background data once the Earthshine is removed.

3.1 Background Information and Field Selection

The contribution and variation of background light in Hubble images is a complex combination of various factors. Variable foreground emission of sources like Earthshine, Moonshine, Sunshine and Zodiacal light combine with intrinsic factors related to physical baffling of the instrument, optical design and pointing of the instrument.

In this study I use data from the North and South Great Observatories Deep Origins Survey (GOODS) [Giavalisco et al., 2004] and the Cosmic Evolution Survey (COSMOS) [Koekemoer et al., 2007]. These were selected because they are deep imaging fields, which have: (1) a lot of imaging data taken over many epochs, (2) no extended or bright sources in the field, (3) similar bandpasses to SkyHopper and (4) a range of ecliptic latitudes to probe different Zodiacal strengths.

Temporal variation in Zodiacal light is expected over the duration of a set of observations. I identify at least 2 epochs of observations for each of the 3 fields over 2002 to 2004 in order to explore temporal variation. A range of ecliptic latitudes was used to decouple the relationship between background emission and Zodiacal light variation. Placement of these fields is shown in figure 3.1.

3.2 Hubble Archival Data Extraction and Preparation

Processed archival quality control data from the Instrument Science data base 'StarView' was used collate information about the sky background observed by Hubble with pointing information. The parameters used in this study are summarised in table 3.1. These parameters are used to explore the relationship between environmental parameters such as observed background, with the pointing of the instrument I will define as orbital parameters. The environmental parameters will then be used to derive a relationship between the Earthshine beneath the telescope, and the background observed by Hubble.

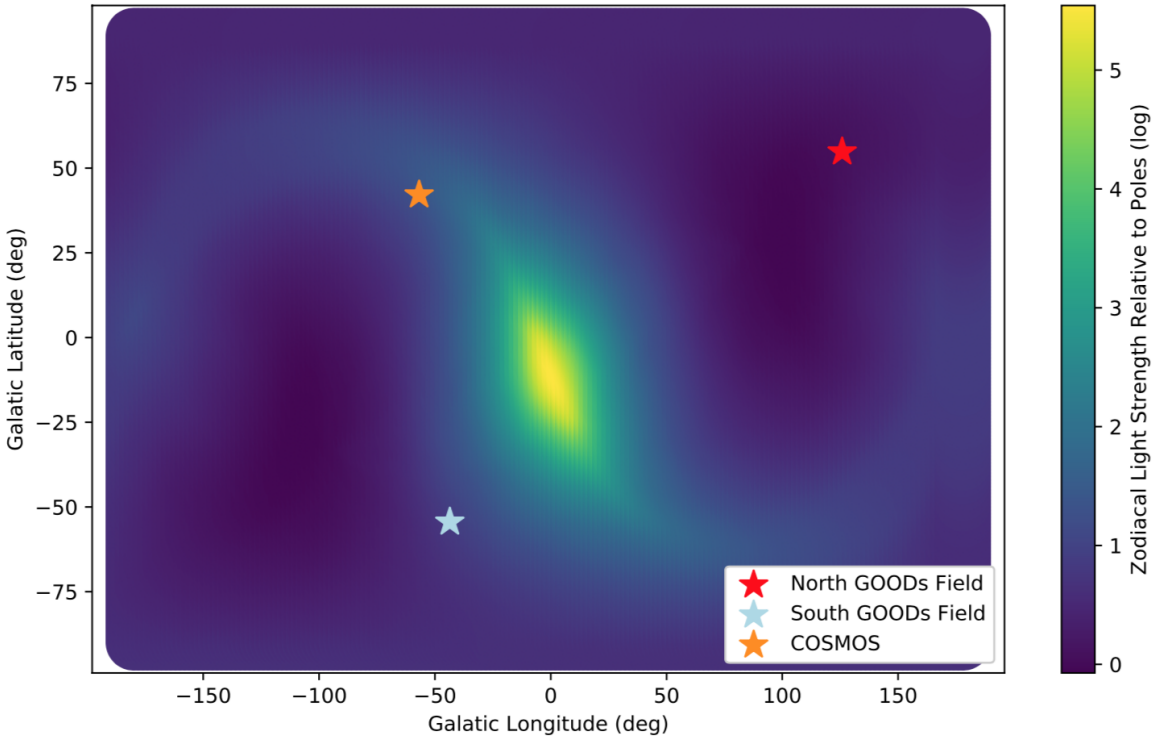

Figure 3.1: Location of fields selected for this study with respect to the relative Zodiacal light strength from the ecliptic poles. To better understand the relationship between seasonal Zodiacal light variation and Earthshine contamination a range of ecliptic latitudes were used.

Parameter	Description
Solar Vector	The vector defined by the line of sight from the telescope to the Sun
Earth Limb Vector	The vector defined by the line of sight of the telescope to the Earths limb
Field Vector	The vector defined by the line of sight of the telescope to the field
Sun Altitude	The angle of the solar vector with respect to the Earth Limb vector in degrees
Sun Angle	The angle between the Solar vector and the Field Vector in degrees
Sky Background	The averaged sky background as computed by Astrodrizzel in units of e^-/pix. See subsection 3.2.1 for details
Moon Angle	The minimum line of sight between the field vector and the vector defined by the line of sight of the telescope to the Moon in degrees
Limb Angle	The angle between the field vector and the Earth limb vector in degrees
Altitude	The altitude of the telescope above the Earth's surface in kilometers at the start of an exposure

Table 3.1: Definitions of the parameters used in this study to correlate Hubble pointing information with observed background.

3.2.1 Calibration of Background Flux

Hubble imaging products undergo an automated sky background subtraction with the `Astrodrizzel` function in STScI `Drizpack` software [Hack et al., 2019]. The sky background value is computed via a processes of sigma clipping pixels with extreme values. After five iterations, the standard deviation of pixel values is computed, and pixels deviating from the mean value by more than 4σ are rejected. The median value of non-rejected pixels is the adopted estimate

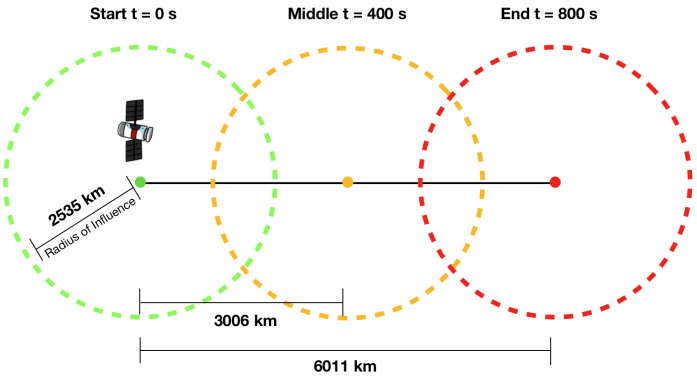

Figure 3.2: Hubble's 800s orbit is broken into 3 overlapping projected regions on the surface of the Earth. These regions will be used to identify the Earthshine most likely to scatter into the aperture of the telescope.

of the sky background level.

The sky background estimates are given in units of un-calibrated instrumental flux e^-/pix [Fruchter and Sosey, 2009]. For each observation, the zeropoint can be derived for the specific instrument configuration given photometric header keywords. `PHOTFLAM` and `PHOTPLAM` are used representing the scaling factor necessary to transform an instrumental flux in units of e^-/s to a physical flux density [Fruchter and Sosey, 2009]. The average sky subtracted background can then be represented in terms of physical flux densities in photlam units $(ergs/s/cm^2/Angstrom)$.

3.3 Deriving the Requirements for Earthshine Correlation

The SkyHopper mission will have roughly the same orbital altitude as Hubble, which currently has an average altitude of 540 km. The portion of the Earth's surface (and hence the approximate source of Earthshine) is therefore similar for the two telescopes. To calculate the region that can contribute to Earthshine, I assume an Earth radius of 6370 km. In the calculations, Hubble's altitude at the start of an individual exposure is used. The radius of influence is defined to be the distance to the horizon on earth from Hubble's altitude. This is found by:

$$R_{Earthshine} = \cos^{-1}\left(\frac{R_{Earth}}{R_{Earth} + Alt}\right) \times R_{Earth} \tag{3.1}$$

Corresponding to an average radius of influence of 2535 km. Earthshine scattered from the circular region projected onto the surface of the Earth defined by this radius and refered to as the region of influence.

To simplify the analysis, the duration of each exposure analysed was restricted to $\sim 800s$ to reduce the number of weather systems that contribute to the Earthshine appearing in the Hubble imaging [Giavalisco, 2002]. Hubble's orbit is approximately 90 minutes in duration, thus for each 800s exposure Hubble traverses approximately 15% of its orbit. Assuming a circumference of the Earth of 40075 km, Hubble traverses a projected distance of 6011 km on the surface of the Earth during each 800s exposure.

As shown in figure 3.2, each exposure is associated with 3 circular regions below Hubble on the Earth's surface that correspond to the beginning, middle and end of an exposure. These 3 overlapping regions will be used to identify the Earthshine most likely to scatter into the aperture of the telescope.

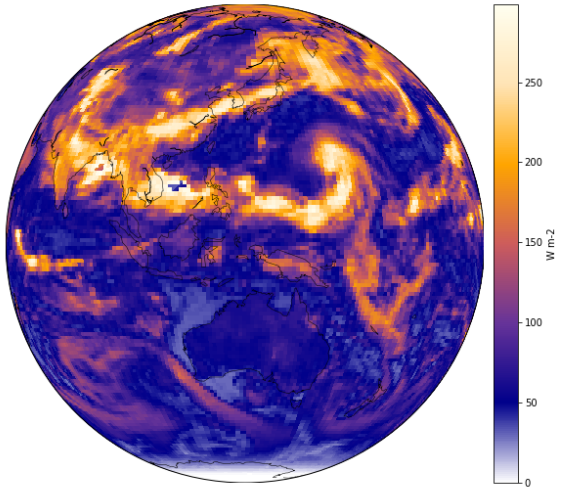

Figure 3.3: The Earthshine as seen from the top of the atmosphere from CERES satellite data. An animated version of this is available here, which shows significant variation in Earthshine over November 2002 when some of the North GOODS data was taken by Hubble. For a static example over 6 days, see A.6.

3.4 Hubble Ephemeris Data and Location Tracking

The location of Hubble above the Earth is only available in FITS headers of fields for the beginning of an exposure. In order to determine the location of the telescope above the Earth for the entire duration of the exposure, the ephemeris for Hubble needs to be known, and updated for each exposure.

Archived North American Aerospace Defense Command ephemeris data for Hubble over the past 20 years was used for this study. The python package `pyephem` was used to determine the Earth's longitude and latitude below the telescope for the start, middle, and end of the exposure to derive Hubble's location.

3.5 Preparing Satellite Earthshine Data

The corresponding Earthshine (specifically top of the atmosphere upwards flux in the context of CERES) for each Hubble exposure was estimated using NASA satellite weather data. NASA's CERES survey is an ongoing study that has been monitoring the Earths incoming and outgoing radiation for more than 30 years [Leob and Kizer, 2019]. It is based around data products from a fleet of NASA satellites: TERRA, AQUA, VIIRS and MODIS. The data is publicly available and contains historical information about the upwards flux present for all Hubble observations. By correlating this data with the background flux in an individual Hubble image, an understanding of the impact of Earthshine in Hubble fields can be derived.

Top of the atmosphere upwards flux data products (Edition 4.0) provide global maps with radiative fluxes (in W/m^2) and cloud properties spatially averaged onto a uniform grid divided into $1^\circ \times 1^\circ$ latitude - longitude regions. These data products provide coverage both hourly, daily and monthly [Loeb et al., 2018]. Using the python package `NETCDF4`, CERES HDF4 files can be opened and queried by date, longitude and latitude. CERES bandpasses used are compared to Hubble bandpasses in figure 3.4.

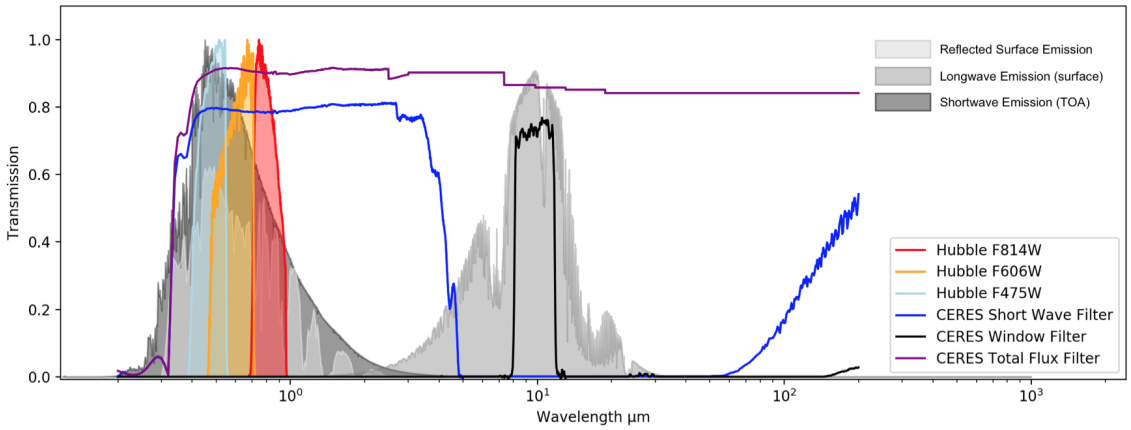

Figure 3.4: The location of CERES broadband and narrowband filters with respect to reference ACS Hubble filters. The reflected surface emission with absorption features from the atmosphere is shown in light grey. The thermal emission (longwave) from the surface and top of the atmosphere (TOA) shortwave emission is also shown for reference. Only CERES shortwave filters are used in this work to prevent influence of longer wavelength emission outside of Hubble's sensitivity range.

3.6 Corrections Due to Hubble's Attitude

Hubble is never pointing at the ground, so the field location with respect to the Earth will impact what portion of light that will scatter from the Earth into the telescope as shown in Figure 3.5. Therefore, a pointing vector must be projected onto the Earth in order to determine the sector of the region of influence that is most likely to scatter into the telescope aperture.

Data from CERES top of the atmosphere upwards flux maps are selected based on an algorithm developed during this thesis to calculate the Earthshine background scattered into the aperture. As shown in Fig 3.4, a region on the surface that is +/-45 from the pointing vector is used to define the Earthshine most likely to scatter into the telescope aperture and will be referred to as the "sector of influence". In this work, this angle does not depend on limb angle of the telescope. Future work is needed to derive relationship between the limb angle and the defined sector of influence.

To derive the Earthshine beneath the telescope, first the location of Hubble is projected onto the surface of the Earth. The right ascension and declination of the field during the exposure provided by StarView is then used to compute the altitude and azimuth of the field given an observer on Earth. The azimuth of the field can be treated as a rough bearing with which the direction of the pointing vector is determined as shown in figure 3.5.

A two-stage boolean iteration loop was used to identify the CERES data that fell within the desired sector of influence. For each $1^\circ \times 1^\circ$ "pixel" on the CERES grid, the distance from the location directly below Hubble was computed:

$$d = 2R\ atan2\left(\sqrt{h}, \sqrt{(1-h)}\right) \tag{3.2}$$

where:

$$h = sin^2\left(\frac{\Delta\phi}{2}\right) + cos\,(\phi_1)\,cos(\phi_2)\,sin^2\left(\frac{\Delta\theta}{2}\right) \tag{3.3}$$

and ϕ is latitude, θ is longitude and R is the radius of the Earth. The geometry of the problem

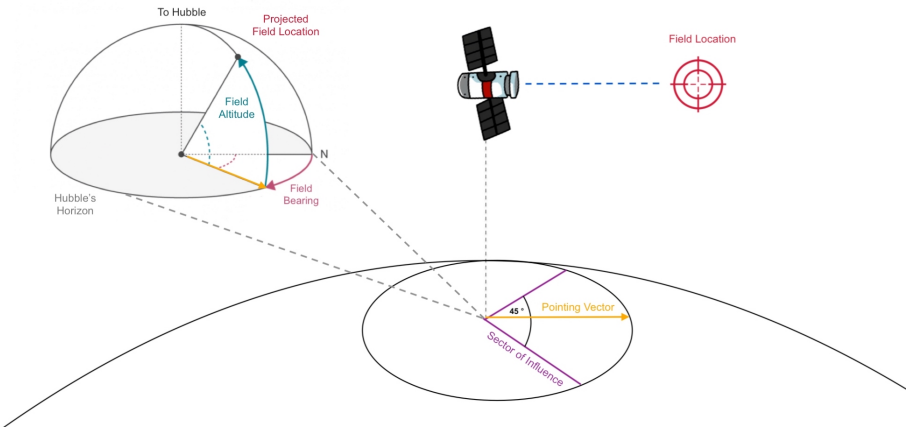

Figure 3.5: The azimuth of the field with respect to Hubble's projected location on the Earth is computed at the time of observation and serves as a bearing to determine the direction of the pointing vector with length equal to the radius of influence, and in the direction of Hubble's line of sight.

is shown in figure 3.6.

If a given CERES pixel with distance d from the point below Hubble is inside the radius of influence (i.e. the CERES pixel is observable by Hubble), next the angle between the pointing vector ($\vec{b}$) the CERES pixel ($\vec{a}$) and Hubble's location (U) is computed using Haversine's rule of spherical cosines.

The angle between the pointing vector ($\vec{b}$) and the test point (V) is then Θ given by:

$$cos(\vec{c}) = cos(\vec{a})\,cos(\vec{b}) + sin(\vec{a})\,sin(\vec{b})\,cos(\Theta) \tag{3.4}$$

Applying the two requirements outlined above to test point (V) (i.e. $d < r_{influence}$ and $-45 < \Theta < +45$), all remaining pixels within the final "sector of influence" are averaged and used in Earthshine analysis.

3.7 The Impact of Orbital Parameters on Observed Sky Background

The orbital parameters that will be derived for SkyHopper in order to avoid Earthshine contamination are: (1) the minimum limb angle and (2) the minimum Sun altitude. A limitation of the following work is that each field is imaged with Hubble over a limited period of time (4 to 12 days in this case) the Sun angle does not vary significantly. In any case, SkyHopper will likely adopt a standard Sun angle of between 45 and 135 degrees.

In this study, I select two periods of consecutive observation for each of the 3 fields. These periods of observations, and respective Zodiacal light variation can be found in Figure A.3 and Figure A.4.

3.7.1 Limb Angle and Sun Altitude

The relationship between Sun altitude and limb angle are explored in detail, shown in figure 3.7. Each field is presented separately, as the complex relationship between Sun altitude and limb angle depends on the field location and the position of Hubble in its orbit.

The North GOODS field has the lowest overall sky background in individual images. This is due to its position highest off the ecliptic plane and therefore lowest Zodiacal light

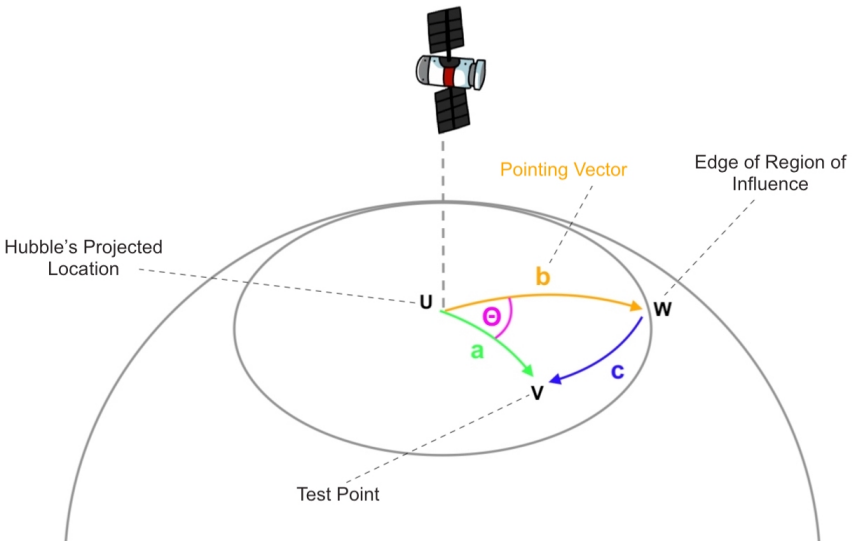

Figure 3.6: The geometry of the algorithm used to select only Earthshine data from CERES that is located within in Hubble's projected radius of influence. It must also be within the 90 deg sector of influence defined by the pointing vector $\vec{b}$ in the direction Hubble is imaging.

variation of the period of observation (see Figure 3.1). Due to the high limb angle of the North GOODS field, the background remains minimal to Sun altitudes of as high as 80 degrees. We see clearly however, the effects of Earthshine at a limb angle of 50 degrees and Sun altitude of 100 degrees.

The South GOODS field is lower on the ecliptic plane to the North, and is expected to have higher Zodiacal light contamination and we see it has an overall higher average background than North. For this field, pointings are clustered into 4 groups. The variation in Sun altitude and limb angle for the 4 pointings are a result of a mosaic over the course of the set of observations. We see a similar result to the North fields with high Sun altitudes and low limb angles resulting in higher backgrounds.

Finally for the COSMOS field there is no clear relationship between the background observed and the Sun and limb angles. The cosmos fields sits low in the ecliptic plane and so has the highest Zodiacal light contamination and also has the highest background of all the fields.

To summarise Figure 3.7, for high ecliptic latitude fields (where we will observe COIB), Sun altitude and limb angle are found to be the most important orbital parameters in determining how much Earthshine appears in Hubble sky backgrounds. This relationship is perturbed for lower ecliptic latitude fields which have appear to have no relationship between observed background and orbital parameters. These fields have elevated sky backgrounds due to expected Zodiacal light contamination.

To further explore this relationship with the most strongly correlating parameter Sun altitude, I plot the background observed as a function of Sun altitude for the North GOODS and South GOODS fields in figure 3.8. Shading in this figure represents the time the exposure was taken, with light colours as the start of the set of observations, and darker colours at the end, highlighting a gradual decrease in background for each pointing over time. I calculate the expected Zodiacal light intensity in each field for the date of exposure at the start and end of the set of observations. This is performed by multiplying the north ecliptic pole scaling constant calculated by the python package `Gunagala` (see section A.1) for the time, date of the exposure and location of the field, with the expected NEP Zodiacal light intensity in the

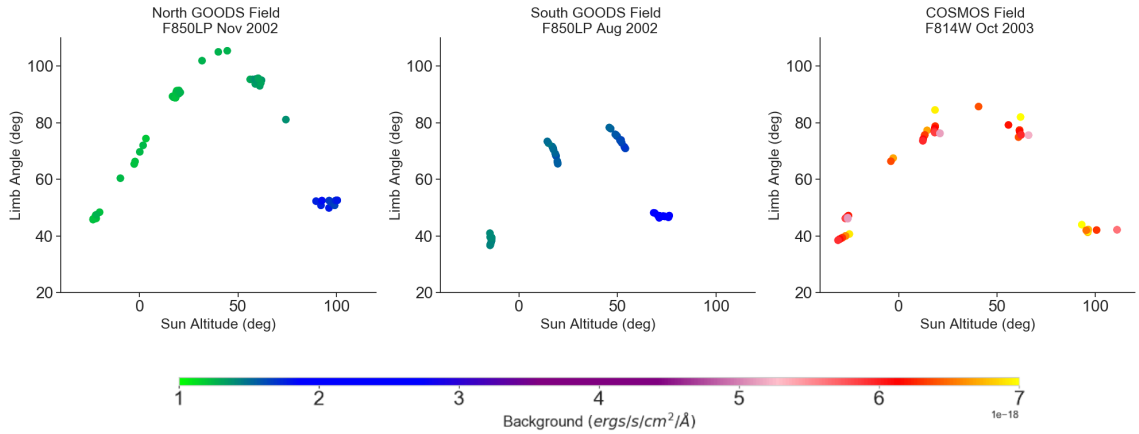

Figure 3.7: The limb angle as a function of Sun altitude for individual exposures in each of the 3 fields explored in this work. For the North GOODS fields with the highest ecliptic latitude and lowest Zodiacal light contamination, exposures of high Sun altitude and lower limb angles clearly result in the highest detected sky background in individual images. The relationship is less clear for the COSMOS field which is highly polluted with Zodiacal light due to its low ecliptic latitude.

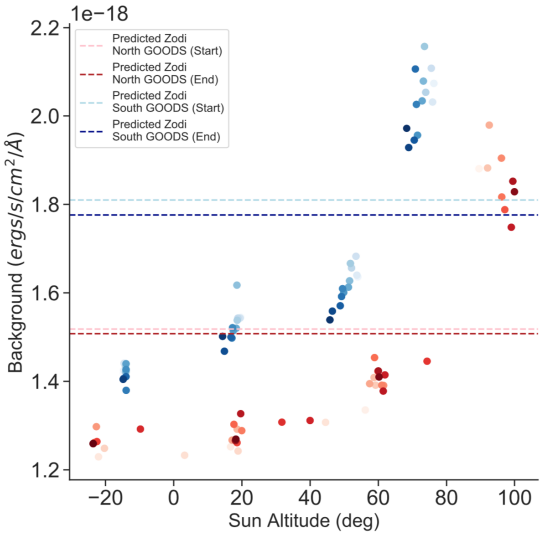

Figure 3.8: The background observed as a function of Sun altitude for the North GOODS and South GOODS fields. Shading represents the time the exposure was taken, with light colours as the start of the set of observations, and darker colours at the end. Dotted lines indicate the predicted intensity of Zodiacal light at the beginning and end of the set of exposures. The conclusion is that there is a clear relationship between Sun altitude and background for both fields, which is being perturbed by the temporal variation in Zodiacal light intensity.

corresponding bandpass given by Giavalisco [2002]. The decreasing trend observed in the data matches the decrease in Zodiacal light intensity predicted by `Gunagala` algorithms.

This figure highlights the fact there is a clear relationship between Sun altitude and the observed background of a field. It also indicates a temporal variation background intensity corresponding to the time and date of an exposure which appears to correlate with the predicted Zodiacal light intensity of the field.

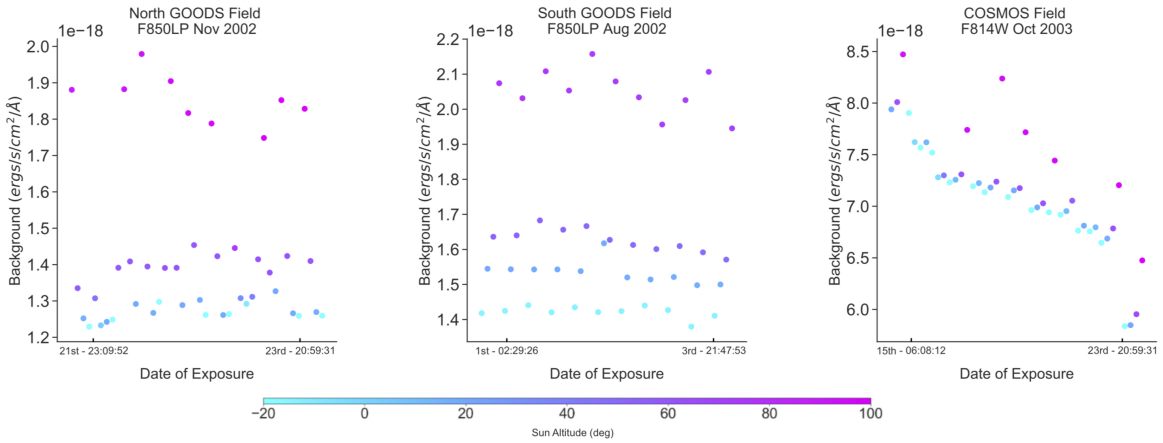

Figure 3.9: Background detected in Hubble fields as a function of time. As established in Figure 3.7, background is found to be highly correlated to Sun altitude in all 3 fields due to Earthshine contamination at higher Sun altitudes. The COSMOS field also shows strong evidence of direct influence of Zodiacal light variation on detected background over a time period as short as 8 days. This result follows the decreasing trend computed using Gunagala and shown in Figure A.3

3.7.2 Temporal Variation in Observed Background

To explore the impact of temporal Zodiacal light variation on the background, I plot the background as a function of the date of the exposure in figure 3.9. At fixed Sun altitudes we see little trend in background for the North GOODS fields as expected from the conclusions of figure 3.8. Indeed, by limiting the North GOODS field to exposures below a Sun altitude of 0 to reduce the Earthshine contributions results in an average fluctuation in background of 1.63%.

In contrast, for the COSMOS field, the variation in background with respect to time and date is more significant likely due to its lower ecliptic latitude and stronger Zodiacal contributions. The correlation with time agrees with theoretical predictions for Zodiacal light seasonal variations as shown in figure A.3. Limiting fields to only those below a Sun altitude of 0 degrees results in a fluctuation of 6.58%, which as expected is higher the North GOODS fields.

3.7.3 Indications of Zodiacal Light Contamination

I perform the same analysis to the COSMOS field as has been presented in Figure 3.8. I identify 8 sets of observations over an 8 day period and calculate the expected Zodiacal light intensity plotted as dashed lines shown in Figure 3.10a. The result of this analysis confirms the perturbations to the relationship between Sun altitude and background to be due to the rapid change in Zodiacal light intensity over the 8 day period. This is calculated to be a 20.58% decrease in Zodiacal light intensity over an 8 day period, or 0.16% per orbit.

In figure Figure 3.10b I calculate the expected Zodiacal light intensity for every observation individually, and subtract this value from the observed sky background. Earthshine contamination is still observed for fields of Sun altitudes. Positive and negative residuals are observed below a Sun altitude of 0 where little Earthshine is expected. These offsets from predictions indicate that current Zodiacal light modeling algorithms may be unable to accurately predict variation in Zodiacal light.

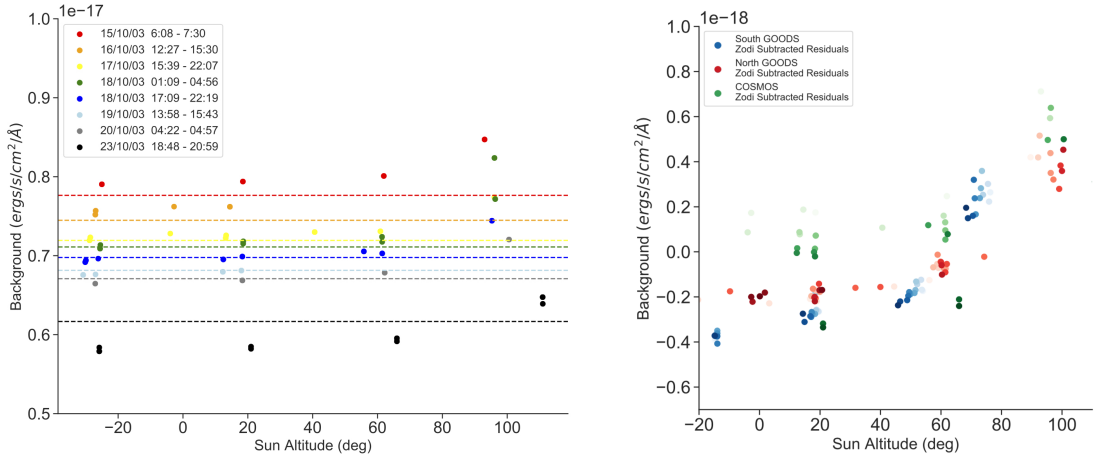

(a) (b)

Figure 3.10: *Left*: Observed sky background as a function of Sun altitude for the COSMOS field. The 8 day period of observations is broken into 8 sets. For each set a predicted Zodiacal light intensity is calculated and plotted as a dotted line. Zodiacal light predictions appear to match the data for each set. For each set, background increases as expected for higher Sun altitudes. *Right*: The result of subtracting predicted Zodiacal light intensities for all 3 fields. Shading in this plot corresponds to the date of the exposure. Higher Sun altitudes exhibit higher backgrounds due to the presence of Earthshine after Zodiacal light subtraction in all 3 fields. Residuals for Sun altitudes below zero are not centered about a zero background intensity (some are lower than zero) indicating that current methods of Zodiacal light prediction are only rough estimates.

3.8 Predicting Earthshine Intensity from Weather Data

I now explore the potential for a relationship between independently sourced CERES weather data with Hubble observed sky backgrounds.

The high correlation between Earthshine, Sun altitude and limb angle provide a means of exploring pointing constraints that reduce the contamination due to Earthshine. By taking the mean and standard deviation of observed sky background selected to only contain observations within certain Sun angles and limb angles, SkyHoppers pointing constraints can derived.

The lowest mean and standard deviation of observed sky background occurs at a Sun altitude limit of no greater than 0 and a limb angle of no less that 35 degrees. Table 3.2 shows the results before and after applying this condition to all fields which results in a reduction in the mean sky background and a marked reduction in the standard deviation of sky background. As a result, the restriction on orbital parameters for SkyHopper will be defined as: (1) limb angle $>$ 35 degrees and (2) Sun altitude $<$ 0 degrees.

In figure 3.11, the measured Hubble background for North GOODS fields is shown as a function of CERES upwards flux. North GOODS is chosen due to its highest ecliptic latitude and least Zodiacal light contamination.

Accepted observations (black) have consistent background levels, which reflects the fact that they may successfully avoid Earthshine. Rejected observations (red) are found to follow a positive linear trend with CERES observed fluxes. This positive trend might be expected in a scenario where fields of highest background levels are those with the highest Sun altitudes and hence the strongest Earthshine levels. There is still significant scatter resulting in a chi squared value for the linear fitting of 0.44.

The findings based upon figure 3.11 suggest that the algorithm defined in this thesis to correlate CERES upwards flux measurements with Hubble sky background could be used

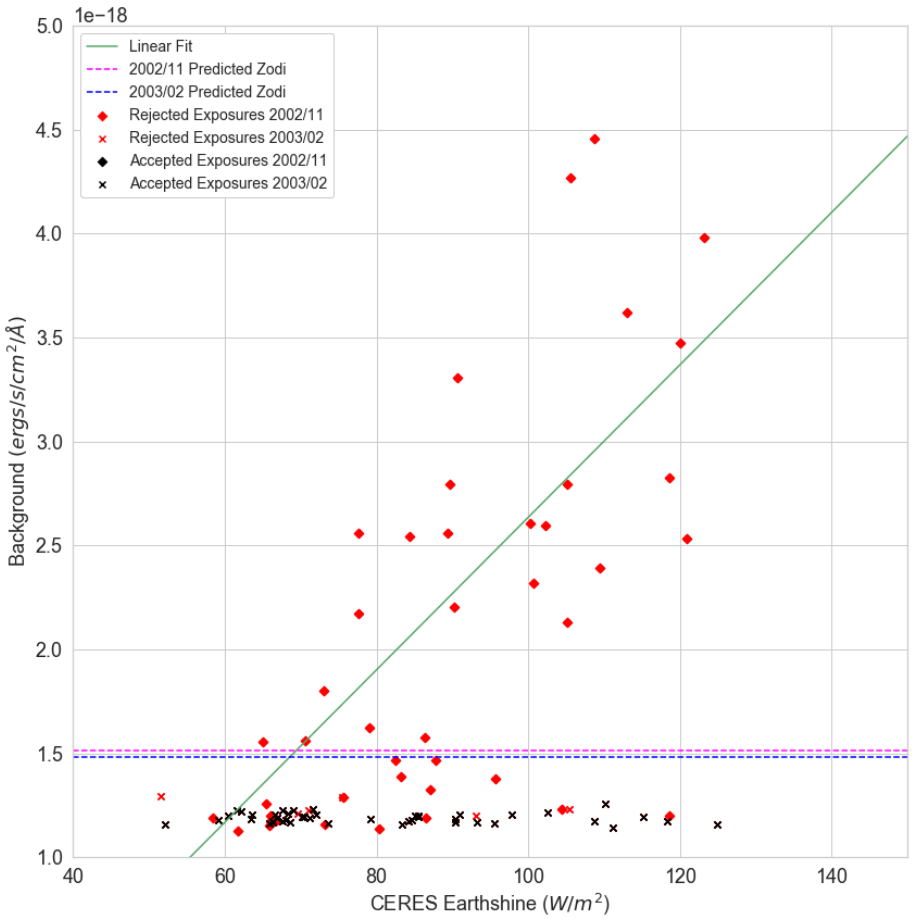

Figure 3.11: Hubble background as a function of CERES weather satellite data. Red diamonds and crosses are rejected fields that do not meet the pointing constraints of limb angle > 35 degrees and Sun altitude < 0 degrees. Back diamonds and crosses are fields that do meet this criteria. The pink dashed line is the predicted mean Zodiacal light background for North GOODS fields taken in November 2002. The dashed blue line is the predicted mean Zodiacal light for North GOODS fields taken in February of 2003. The green line is the linear fit for Hubble detected sky background as a function of CERES detected Earthshine for rejected exposures. Selecting fields within SkyHoppers derived pointing constraints ensures only fields that are not contaminated with Earthshine are considered. A linear relationship between CERES flux and Earthshine contaminated Hubble fields is present, which may lead to the ability to predict fields of highest risk of Earthshine contamination

to predict regions of SkyHopper's orbit that have the potential for high risk of Earthshine contamination.

3.9 Conclusions

As a result of this study, I find that the Sun altitude with respect to the position of a space telescope in its orbit is the orbital parameter that most influences the detection of Earthshine in an exposure. Limb angle is also found to be an important factor in deriving pointing constraints for SkyHopper.

I show that by adopting strict Sun altitude and limb angle constraints, the impact of Earthshine variability and detected stray light can be reduced. This results in the sky background percentage variance to be improved by as much as ~ 50%.

I derive pointing restriction for SkyHopper to avoid the influence of Earthshine of a limb angle avoidance of no less than 35 degrees, a Sun altitude of no greater than 0 degrees which will be utilised during observations of the COIB.

Field	μ Before	σ Before	μ After	σ After	Zodi Prediction
North 2003/02	1.195e-18	3.333e-20	1.183e-18	2.344e-20	1.482e-18
North 2002/11	2.045e-18	9.230e-19	NA	NA	1.513e-18
South 2003/02	1.411e-18	2.191e-19	1.265e-18	2.110e-20	1.825e-18
South 2002/08	1.646e-18	2.369e-19	1.419e-18	1.587e-20	1.788e-18
COSMOS 2003/10	7.067e-18	6.199e-19	7.009e-18	5.456e-19	7.080e-18
COSMOS 2004/04	2.229e-18	8.538e-20	2.189e-18	4.161e-20	2.919e-18

Table 3.2: The mean and standard deviation of detected background in units of $ergs/s/cm^2/$Å before and after imposing limb angle and Sun altitude constraints. The mean sky background observed and standard deviation of the sky background decrease (in most cases standard deviation decreases by an order of magnitude) when imposing these constraints. Zodiacal light prediction is shown for comparison to the mean sky background. This table shows that the percentage variance of the observed sky background can be improved by as much as $\sim 50\%$ with the use of pointing constraints.

For this work, I created novel algorithm and package in Python to obtain Earthshine measurements beneath a low Earth orbiting space telescope. It is designed to capture the intensity of stray light from Earthshine. While archival data was used for this study, its plausible to run it in real-time with live CERES climate monitoring satellite data as a means of quantifying Earthshine beneath any space telescope.

I also highlight a possible disagreement between predicted and observed Zodiacal light levels. These inconsistencies are as high as 8.91%, which are problematic for using the existing theory predictions for removing a Zodiacal component from SkyHopper COIB measurements. This provides strong evidence and motivation towards the need for direct accurate detection of the strength of the Zodiacal light foreground in the SkyHopper mission.

4

Direct Measurement of Zodiacal Light

Zodiacal light is the dominant source of foreground emission in for telescopes in low Earth orbit and is the main source of error for direct photometric measurements of the COIB [Bethermin, 2011], and indeed in chapter 3, I show that Zodiacal Light emissions make up a significant fraction of the background observed by Hubble. Unlike Earthshine, there is no way of avoiding this emission with the use of orbital constraints, and as a result Zodiacal light must be measured directly as described in chapter 2. In this chapter, I explore the instrument requirements needed to measure the Zodiacal light strength with SkyHopper narrowband filters to the goal of 0.1% in order to achieve a measurement of the COIB to within a 1% level of accuracy.

4.1 Science Case Field Selection

The COIB science fields are chosen to be the same as those used for the CIBER mission [Tsumura et al., 2010]. These fields are selected to be high off the ecliptic plane to reduce the intensity and variability of Zodiacal light emissions. Galatic latitude and longitude of the selected fields are given in table 4.1. The CIBER Boötes fields have been studied in detail with the Infrared Array Camera (IRAC) shallow survey on the Spitzer Space Telescope [Eisenhardt et al., 2004, Tsumura et al., 2010]. This provides infrared maps of bright sources, as well as maps of galactic cirrus for cirrus subtraction used by the CIBER team (see Tsumura et al. [2010] and Arai et al. [2015]) Similarly, the SWIRE ELIAS-N1 field was observed as part of the SWIRE survey conducted by Spitzer, and is an ideal target given SWIRE's focus on selecting fields to minimize galactic cirrus emissions over large scales [Lonsdale et al., 2003]. The North Ecliptic Pole (NEP) field observed by the CIBER team has also been studied with the AKARI [Matsuhara et al., 2006] infrared space telescope and was chosen because of the fields low density of stars and minimum Zodiacal light foreground.

4.2 Variability of Zodiacal Light Intensity

As outlined in section 2.3, a pair of narrowband filters will be used to constrain the Zodiacal light strength. The maximum total exposure time for these narrowband measurements is set by the rate of change in Zodiacal intensity in that field. Eventually the Zodiacal light intensity in the line of sight of a science field will change in strength, which means we must be able to constrain it before it changes too much. In order to reach our goal of detecting the COIB to 1%, we must securely measure the strength of the Zodiacal light before it changes by 0.1%. We chose a constraint of 0.1% to account for the error budget of other statistical errors in the measurement. See Matsuura et al. [2017] (table 4) for details on CIBER's error budget.

I derive the observing windows for each field by identifying the period of a year where Zodiacal light intensity is the lowest and the percentage change in Zodiacal light intensity is the lowest for each field. The field visibility will also be taken into account and is explored

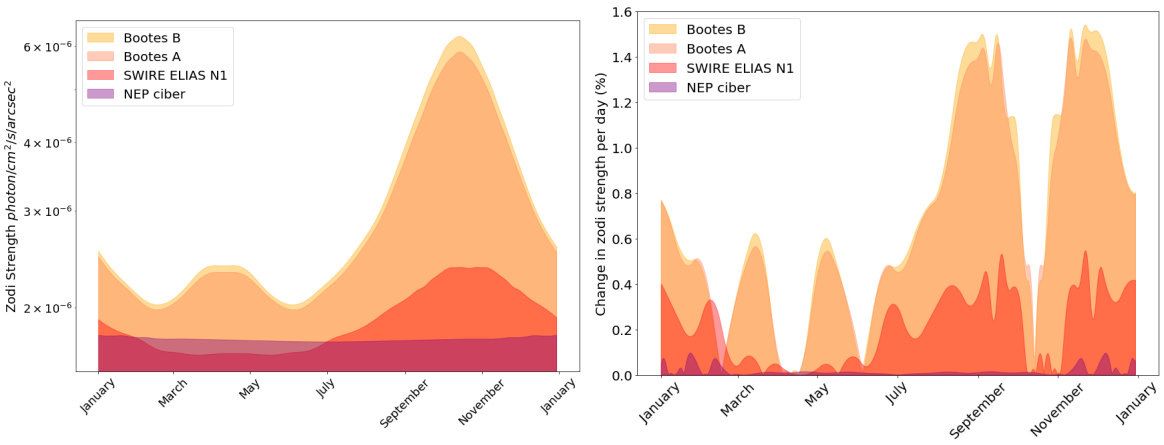

(a) (b)

Figure 4.1: *Left*: Strength of Zodiacal light for each field over the course of the year 2022. This highlights the existence of observing windows for fields where Zodiacal light intensity is the lowest during the year. Observations will coincide with these observing windows *Right*: The derived absolute percentage change in Zodiacal light intensity per day over the course of 2022. Periods of lowest Zodiacal light intensity appear to coincide with period of lowest Zodiacal light intensity, further highlighting the need for identifying appropriate observing windows.

Field	λ	β	Max Change	μ	σ	Δ / Orbit	Max Exp
NEP CIBER	...	90	0.098	0.018	0.021	0.006	588
SWIRE ELIAS-N1	208.40	72.63	0.549	0.207	0.154	0.034	106
Boötes-B	202.23	47.28	1.541	0.709	0.468	0.041	88
Boötes-A	201.23	46.28	1.484	0.680	0.441	0.041	88

Table 4.1: Tabulated results for the percentage change in Zodiacal light intensity per day for the 4 proposed fields. (λ, β) are the ecliptic coordinates of the field in degrees taken from Tsumura et al. [2010]. *Max Change* is the maximum percentage change in Zodiacal light intensity per day in $ergs/cm^2/s/\text{Å}/arcsec/day$ for the entire year. (μ, σ) are the mean and standard deviation of the percentage change of Zodiacal light intensity per day in $ergs/cm^2/s/\text{Å}/arcsec/day$ for the identified observing windows in shown in 4.3. Δ*/orbit* is the percentage change of Zodiacal light intensity per orbit in the identified observing windows. *Max Exp* is the maximum total exposure time allowed before the intensity of the Zodiacal light changes beyond 0.1%.

in section 4.3. Similarly to chapter 3, in figure 4.1a I calculate the Zodiacal light surface brightness relative to the ecliptic pole for the given field each day over the year 2022, the first year of observations for SkyHopper after launch.

The relative Zodiacal light intensity for the specific field is used to normalise the Zodiacal light SED (see Table A.1 for details) by the NEP Zodiacal light value reported by Hubble's F606W [Giavalisco et al., 2002]. The resulting appropriately normalised Zodiacal SED is convolved with the narrowband filters and system throughput to produce expected flux levels used in the following analysis. This calculation takes into account the annual variation in Zodiacal light distribution as the Earth orbits the Sun. Second order effects such as the inclination of the Earths orbit relative to the plane of the Solar System's dust disk is not taken into account. As a result figure 4.1a highlights how rapidly the Zodiacal light changes towards a given field over the course of a year.

The resulting Zodiacal light strength for each field is then differentiated with respect to time in 24 hour blocks to derive the percentage change in Zodiacal light strength per day, and per 90 minute orbit.

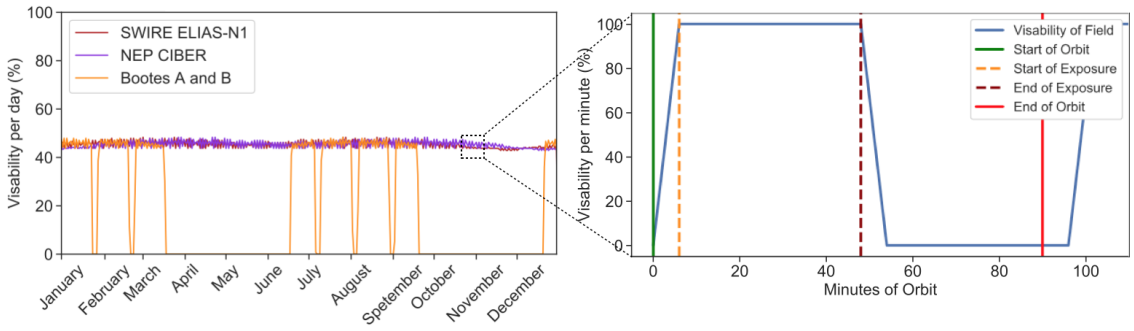

Figure 4.2: The visibility of the 4 target fields over the course of the first year of SkyHopper observations. Derived Orbital constraints to avoid Earthshine derived in Chapter 3 mean that all fields experience a maximum of 40% viability year round. Bootes fields lower ecliptic latitude means that it suffers periods of 0% visibility for half the year. The zoom axis to the right shows the structure of a single orbit, allowing for a maximum of 36 minute observations per orbit.

I define the maximum exposure time of each field as the amount of time it takes for strength of the Zodiacal light to change by 0.1%. The field details and results are tabulated in Table 4.1. Bootes A and B fields have the highest Zodiacal light intensity due to their relatively low ecliptic latitudes. As a result, they also have the highest mean relative Zodiacal light strength, and the highest standard deviation from the mean resulting in the highest variability in Zodiacal light strength of the 4 fields. The windows of observation that correspond to the lowest Zodiacal light variation for these fields is between January to July. The maximum exposure time for Zodiacal light intensity measurement in the narrowband is calculated to be 88 minutes. As shown in Table 4.1 this is the lowest exposure time of all target fields and so will be considered as the worst case scenario target field.

Similarly for the SWIRE field, a maximum Zodiacal intensity relative to the poles is reached during the September - January period. The best time to observe this field is therefore between February - June corresponding to a maximum exposure time of 106 minutes. Lastly the NEP field remains fairly similar all year round, and so has no preferred observation period due to seasonal Zodiacal light strength variation. It achieves a 588 minutes maximum exposure time as so will be considered at the best case scenario target field.

As a result, the major constraint on maximum exposure time for narrowband Zodiacal light measurements are therefore the rapid changes in Zodiacal light strength. The fields of most concern are the Bootes fields, which need to have observing windows that correspond to the minimum Zodiacal light strength, and regions where the rate Zodiacal light intensity change is the least. I explore the impact of these implications on the SNR of observations in section 4.5.

4.3 Field Visibility

The pointing restrictions derived in Chapter 3 to mitigate the impact of Earthshine plus the requirement to avoid Sunlight have implications for the visibility of certain fields.

Using the SkyHopper field visibility routine written by SkyHopper Systems Engineer, Mr. Robert Mearns, I calculate the visibility of each of the SkyHopper fields over the year 2022. This is calculated both monthly, and in 6 minute time intervals for a Dawn-Dusk Sun synchronous orbit at 500 km, with pointing restrictions of 35 degrees from the Earth's limb, a recommended moon avoidance angle of 30 degrees and a Sun altitude of 0 degrees. The orbit is also calculated such that the angle between the line of sight of the telescope and the

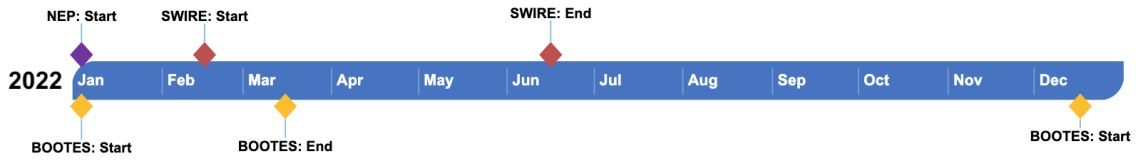

Figure 4.3: The planned observing schedule for the COIB science mission. Diamonds indicate the start and end of the best period to observe each field based upon the Zodiacal light intensity and rate of change derived from the results of Figure 4.1 and the field visibility derived from the results of Figure 4.2

Sun is between 45 to 135 degrees, ensuring the telescope is always pointing away from the direction of the Sun.

The result of monthly calculations are projected onto a Mollweide projection and combined into an animation that can be found here. A static version is provided in figure A.5 for a sample of months. I also plot the visibility of the fields over the course of a year shown in figure 4.2.

Due to their high ecliptic latitude, the SWIRE and NEP fields are not as heavily influenced by the location of the Sun and moon over the course of the year. In contrast, the lower ecliptic latitude BOOTES fields can only be imaged for short periods between mid December to late March. Fortunately this overlaps with the time periods of lowest Zodiacal light intensity and variability. As a result, the visibility of the field over the duration of the year has little impact on narrow band Zodiacal light observations. The planned observation schedule is shown in figure 4.3.

4.4 Probabilistic Modelling and Bayesian Framework

The COIB science case drives a wide-ranging set of instrument and mission requirements. Realistically there will be some amount of descoping to accommodate various factors, including the need to accommodate other science goals. This motivates the need for a way to assess the impact of a particular choice on the final COIB measurement.

A Bayesian model of the instrument was constructed to place constraints on the SkyHopper optical payload design. Eventually this model will encompass all systematic uncertainties that might impact the observations. It will be designed to conduct Bayesian inference on measurements of the COIB given informed priors which define known systematic uncertainties in the process of detecting the signal itself, and in the subtraction of foreground emission like the Zodiacal light. In the following, I present the selection of informed priors that make up the initial model. I also demonstrate the functionality and versatility of the model in providing design constraints for the mission.

4.4.1 Selecting Informed Priors

Bayesian inference is a method of applying probability to complex statistical problems. It is flexible because it easily allows for the updating of a conclusion as more evidence becomes available. In the context of the COIB science case, Bayesian inference will allow us apply what we know about the statistical uncertainties of our system to better draw informed conclusions.

The equation which governs Bayesian statistics is as follows:

$$P(A|B) = \frac{P(B|A)P(A)}{P(B)} \tag{4.1}$$

In this equation and thus the constructed model, we consider B to be the model describing the physical system, which is in this case the SkyHopper optical payload. More specifically, for this initial SkyHopper model, B will be a combination of probability distributions representing the factors such as read noise, dark current and shot noise of the detector system. A represents the true measurement of the COIB intensity in the SkyHopper filters. Here we consider $P(A|B)$ to be the *posterior probability*, the probability that a photon or corresponding photo electron detected by SkyHopper is from the COIB given all the factors, B, that contribute to the probabilistic instrument model. The *posterior probability* will be explored in some detail using the SEDs described in Table A.1 for the Zodiacal light component of the model.

$P(B|A)$ is known as the *likelihood function*. This describes the probability of certain photo electrons measured, given the possible intensities for the COIB at a single wavelength. $P(A)$ is known as the *prior probability*, and is the probability of detecting the COIB at a particular wavelength, with no prior information about the system. Finally $P(B)$ is the *evidence*, or the probability of data.

In this initial model, $P(B)$ will not be considered. This is generally a normalisation term which will be added once SkyHopper observations have been performed.

While this framework will eventually be applied to measure the COIB, for the purposes of this thesis, the framework was used to explore how the requirement of measuring the Zodiacal light translates into technical requirements for the SkyHopper mission. For this initial study to help constrain the science requirements, $P(A)$ will be assumed as a flat, uninformed prior over plausible ranges of parameter values. The term of interest and one which will be explore in depth below is likelihood function $P(B|A)$ of measuring the Zodiacal light given a set of parameters.

The Bayesian instrument model is built in the `PyMC3` (see section A.1) python framework, which allows for flexible definitions of the priors described above. The `PyMC3` model is naturally modular so we can easily constrain further statistical sources of error in the future. In this model, I simulate observations using a Markov Chain Monte Carlo (MCMC) sampling of the defined distributions.

The python-based `PyMC3` module means it is easy to incorporate other python-based astronomy tools such as `astropy`, a custom SNR calculator, `Gunagala` and other misc utilities (see section A.1).

To construct the Bayesian instrument model, statistical processes in the optical payload design can be described with the use of Gaussian priors. Photons registered on the CCD as electrons and arriving within some interval are independent from one another, and so follow a Poisson distribution. For many photo-electrons, we simplify this using a Gaussian distribution, with mean equal to that of the expected Poisson distribution and standard deviation equal to the standard deviation given by $\sigma = \sqrt{N}$ where N is the number of events.

The read noise is an additive noise and can be represented by a Gaussian distribution centered about $\mu_{rn} = 0$ in units of e^-/pix. The expected read noise will vary pixel to pixel, and the quoted read noise value (H_{rn}) is taken as the standard deviation of the read noise distribution across the detector, divided by the square root of the number of pixels in the detector *(bin)* such that $\sigma_{rn} = \frac{H_{rn}}{\sqrt{bin}}$. This is used in the adopted read noise informed prior Gaussian distribution:

$$P(rn) = \frac{1}{\sigma_{rn}\sqrt{2\pi}}\ e^{-\frac{1}{2}((x-\mu_{rn})/\sigma_{rn})^2} \tag{4.2}$$

Some factors to consider are that narrowband observations with SkyHopper have the potential to be read noise dominated because they are unlikely to be sky dominated in the

maximum exposure time available for a particular field in one orbit. Further, read noise decreases with the square root of the number of sub exposures added together. Read noise will also be impacted via the readout mode used and the readout frequency per sub exposure. As a result I will explore the impact of the number of sub exposures per orbit on the achieved SNR and the impact of different read noise values due to the utilisation of various readout modes that may be employed in SkyHopper observations.

The dark current of the detector is a stochastic process which manifests itself as a systematic uncertainty. Dark current, which can be high for infrared-sensors like a Hawaii-2RG is usually calibrated out with dark frames. There is a chance SkyHopper will not be equipped with a shutter because of the risk of having obstructions in front of the telescope aperture once in orbit. If this is the case, it will not be possible to collect in-orbit dark frames for direct characterisation of the dark current variation across the field. On the other hand, if dark current becomes the limiting factor in measuring the COIB, it might be that the risk of incorporating a movable shutter into SkyHopper is warranted.

The baseline plan for observations without a shutter is that reference pixels on the Hawaii-2RG will be blacked out and serve as real-time measures of dark current (H_{dc}). However in the hostile environment of space, pixel to pixel variation across the field is expected to be a significant issue that needs to be captured in this initial model.

I assume perfect dark subtraction on average and therefore only model the pixel-to-pixel variations as a Gaussian distribution centered about $\mu_{dc} = 0$, with a standard deviation defined as $\sigma_{dc} = \frac{\sqrt{H_{dc}}}{\sqrt{bin}}$. Thus, the dark current informed prior is defined similarly to equation 4.2.

Finally I model the shot noise from the light source itself. Again, this is modeled as a Gaussian distribution with the mean as the expected total photon flux μ_{inst} from the instrument in e^-/pix and standard deviation $\sigma_{inst} = \frac{\sqrt{\mu_{inst}}}{\sqrt{bin}}$. The expected instrumental flux is found by:

$$\mu_{inst} = \int F_\lambda \, \epsilon_\lambda \, A_{optic} \, A_{pix} \, d\lambda \tag{4.3}$$

In units of e^-/pix. Here F_λ is the Zodiacal light SED, ϵ_λ is the end-to-end efficiency of the optical system, A_{optic} is the area of the aperture of the telescope and A_{pix} is the area of a pixel in square arcseconds.

4.5 Deriving Initial Technical Requirements

I explore the impact of varying each of the most integral parameters of the Bayesian instrument model, while assuming best estimate values for the variables held constant. In doing so, the impact of instrument constraints and scheduling constraints can be explored in relation to narrow band observations on the Zodiacal light intensity.

I define the SNR of an observation as the mean signal of the binned pixels in the detector in the resulting distribution from `PyMC3` after MCMC sampling for a narrowband observation, divided by the standard deviation of the signal of these pixels. The model incorporates traditional exposure time calculations as well as a non-traditional Bayesian component as a result of the statistical nature of MCMC sampling to simulate a real observation.

To simplify the analysis, the only light source assumed for this work is the Zodiacal light. Future work will incorporate contributions from sources in the field and the COIB. The intensity of Zodiacal light that is assumed in this work is from Giavalisco [2002], which reflects typical level in the CIBER COIB fields as well as upper limits.

In the following, unless otherwise noted I assumed: optimal aperture photometry with a 4 arcsecond point spread function (PSF) FWHM, low Zodiacal light intensity (see Figure A.2,

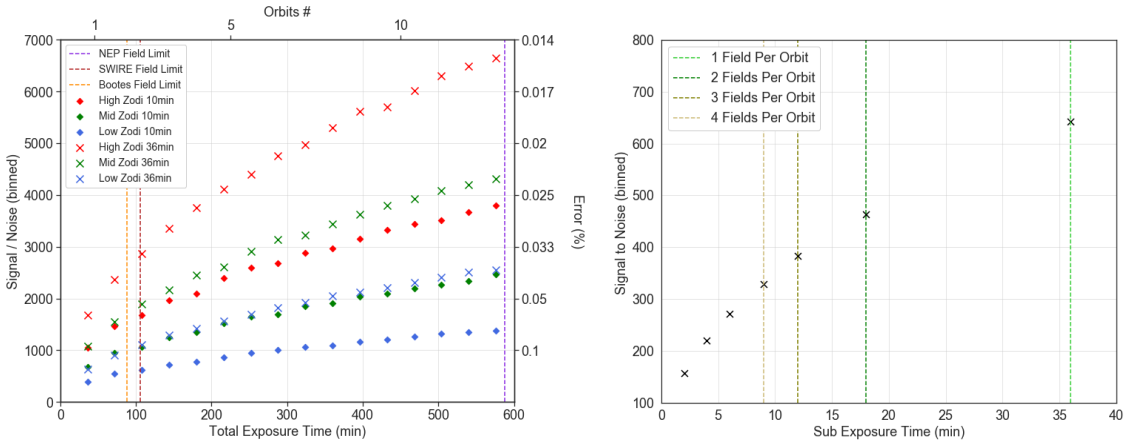

(a) (b)

Figure 4.4: *RIGHT:* The SNR of an observation as a function of total exposure time for 3 Zodiacal light intensities exploring both the longest possible sub exposure time of 36 minutes per orbit (crosses), and a more plausible 10 minutes per orbit (diamonds). Dashed lines indicate the longest total exposure time allowed for that field until Zodiacal light intensity changes by 0.1% given in Table 4.1. The results of this figure are summarised in Table 4.2. *LEFT:* The SNR as a function of sub exposure time over the duration of an single orbit for low Zodiacal light intensity. Dashed lines indicate the SNR achieved per orbit after breaking the orbit up into multiple exposures from 1-7. Observing multiple fields per orbit has a large impact on the SNR achieved, resulting in a decrease in SNR of 28%.

a read noise of 15 e^-/pix and a dark current of $0.01e^-/s/pix$ (see A.2 for details). The SNR value provided is computed using the narrowband filters and methodology outlined in section 2.3.

4.5.1 Total Exposure Time

As outlined in section 4.2, the SkyHopper observations must constrain the Zodiacal light to 0.1% corresponding to a SNR of 1000 in the derived maximum exposure time. If, for example, the necessary time to make a secure measurement is too long, then the physical parameters of the optical payload (such as read noise and dark current) will need to be reconsidered to meet this goal.

To maximised the SNR of an observation, pixels are binned spatially in the narowband field of view. SkyHopper is not concerned with spatial fluctuations of the COIB, so binning spatially is a straight-forward option to increase SNR. The CIBER team aggressively mask pixels to remove stars and galaxies in the field of view. The masking requirements used ensure that the PSF wings of the point sources in the image are less than the statistical uncertainty of the instrument and faint galaxies are masked to a cutoff low enough to allow for the detection of fluctuation in the COIB (see Zemcov et al. [2014] for details on CIBER's masking criteria). As a result of these criteria CIBER mask pixels from 50 - 60% in each image [Zemcov et al., 2014]. I adopt the lower limit of 50% in this work.

I explore the resulting SNR for 3 Zodiacal light normalisation extremes based upon the work by Giavalisco [2002] exploring the entire parameter space. For the 3 chosen fields, only Mid and Low Zodiacal light intensities apply. Figure A.2 shows the scaling of the Zodiacal light spectrum at the calcium triplet for reference and the construction of these SED's is presented in Table A.1. Two possible sub exposure times are used, one where an entire orbit

Field	Low 36min	Mid 36min	High 36min	Low 10min	Mid 10min	High 10min
NEP	2592	4449	6797	1406	2480	3854
BOOTES	994	1688	2575	573	995	1546
SWIRE	1091	1850	2877	607	1058	1654

Table 4.2: The SNR achieved by the proposed fields for the total exposure time derived by Zodiacal light variation for the the best and worst case scenarios for sub exposure time. Boxes highlighted in blue are fields that successfully reach the required accuracy of 0.1% (SNR of 1000) in that total exposure time. Boxes in red are fields that only just reach the requirement and may be at risk if Zodiacal light intensities change more than what is modeled in this work and white boxes are field which don't meet requirements.

is utilised with 40% duty cycle for a 36 min sub exposure time, and a reduced 10 min sub exposure time.

Figure 4.4a shows that the NEP field reaches a SNR of above the nominal target of 1000 even with limited sub exposure times. For an optimal 36min sub exposure time all fields at all Zodiacal light intensities reach the required goal. The SWIRE field is likely to only have low Zodiacal light intensities, so if sub exposure times are limited it will not reach the required SNR. Bootes lower ecliptic latitude may see mid level Zodiacal light intensities leading to a higher SNR and may achieve the required goal at lower sub exposure times.

4.5.2 Sub Exposure Time Per Orbit

In Figure 4.4b I look at the impact of sub exposure time on the SNR of one orbits worth of observation to explore the prospect of taking multiple fields per orbit. I only explore the lowest Zodiacal light intensity limit, as it is the most probable for fields at high ecliptic latitudes where SkyHopper will be make observations, and will be characteristic of the most promising NEP field.

The maximum SNR per orbit for any field with low Zodiacal light intensity scaling is $\sim$ 640 for a 36 minute total exposure time shown in Figure 4.4b. Observing two fields per orbit at 18 minutes each results in an SNR which is 72% of the maximum. Taking multiple fields per orbit, i.e, multiple pointings, is certainly desirable for the Bootes fields. The fields have a short turn around time due to the rapid change in Zodiacal light, and are in close proximity to each-other on sky, but taking multiple pointings has a heavy impact on the achieved SNR.

The result of Figure 4.4b is that maximising the sub exposure time of the observation is key to achieving a higher SNR due to the read noise limited detector, and so observing 1 field per orbit is the best option. In some cases, low sub exposure times may not be avoidable, as SkyHopper must give highest priority to target of opportunity fields and other transient events. Project principle investigator Michele Trent estimates COIB observations will be interrupted once every 14 days on average for target of opportunity events, and so will have little impact on the achieved SNR of fields due to reduced sub exposure times.

4.5.3 Read Noise and Dark Current

Current estimations for HawaII-2RG detector readout noise provided by Teledyne are based upon correlated double sampling (CDS) readout methods. Teledyne report 15 e^-/pix readout at a 100kHz pixel readout rate with an upper bound reported at 30 e^-/pix using CDS. The method of sampling up the ramp (SUTR) has been studied as a solution for low surface brightness imaging which involves sampling the detector multiple times during the duration of the exposure [Benford et al., 2008].

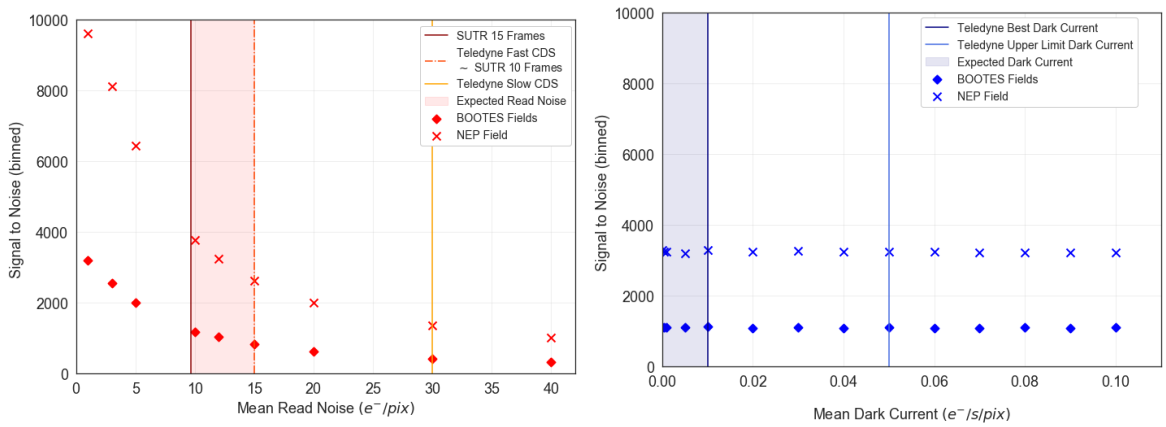

(a) (b)

Figure 4.5: *Left*: SNR vs read noise. Red crosses are NEP fields of 588min total exposure time and red diamonds are BOOTES fields of 88min total exposure time. The shaded red region is where the read noise is expected for the HAWAII-2RG depending upon the chosen frame rate. The dark red line is the best case scenario with 15 samples per read. The dotted orange line is the worst case scenario with 10 frames per read. The yellow line is the upper limit on read noise quoted by the manufacturer. *Right*: SNR vs dark current. Blue crosses are NEP fields with 588min total exposure time. Blue diamonds as BOOTES fields with 88min total exposure time. The shaded blue region highlights the expected region for the HAWAII-2RG dark current. The blue line indicates the goal quoted dark current by the manufacturer. The light blue line is the upper limit on the dark current quoted from the manufacturer.

SUTR is only possible as the infrared HAWAII-2RG detector is capable of non-destructive readout and multiple sampling. This allows for multiple reads during an exposure, which can be used for eliminating cosmic rays during long exposures and reducing the effects of saturation of bright sources [Benford et al., 2008]. I estimate the read noise by SUTR using the following equation from Benford et al. [2008]:

$$\sigma^2_{SUTR} = \frac{12(n-1)}{n(n+1)}\sigma^2_{read} \tag{4.4}$$

A single read is equal to the CDS readout mode read noise divided by $\sqrt{2}$, as CDS involves sampling once at the start of an exposure and once at the end. Thus the single read noise is $\sim 10.6e^-$/pix.

The frame rate is defined as the number of reads (n) conducted per exposure. Due to SkyHoppers limited processing power, SkyHopper project engineer Robert Marens expects a frame rate of 10, possibly extended to 15. A frame rate of 10 results in approximately the same read noise as CDS fast sampling. Pushing to a higher sampling rate of $15e^-$/pix, results in a significant reduction in read noise resulting in $9.69e^-$/pix.

Based upon 4.5a, read noise appears less of an important factor for the NEP, the field that has a long total exposure time. For the BOOTES fields where the total exposure time is short read noise is a more important factor. In order to reach a SNR of 1000, the read noise must be limited to no greater than $12.5e^-$/pix.

The results of the simulations shown in figure 4.5 indicate that dark current is expected to be of little risk to the mission due to its weak impact on the SNR of the narrow band observations as compared to the read noise.

The dark current actually achieved by the detector will be dependant upon the operating temperature of the detector once in space, as well as the quality of the detector including artifacts from manufacturing resulting in pixel to pixel variation. As a result I explore a wide

range of possible dark current values. Similarly to read noise there have been many detailed studies into characterising and quantifying the dark current performance of the HAWAII-2RG due to its use in NIRSpec and NIRCam on JWST. [Mott et al., 2007, Finger et al., 2004, Benford et al., 2008, Loose et al., 2010, Beletic, 2007]

4.6 Mock Observations

A limitation of the current version of the Bayesian framework is that it does not capture how the FWHM of the Point Spread Function impacts the SNR of the Zodiacal measurements. While every effort will be made to reduce the impact of spacecraft jitter on the PSF and tracking errors, there is a chance it will be less than optimal for the science goals. To explore the impact of the PSF size on the Zodiacal light measurement, a series of mock images were created to simulate a COIB field with a realistic distribution of stars of known magnitudes plus a Zodiacal light background.

I perform a cone search on the Sloan Digital Sky Survey (SDSS) DR15 over a radius of 3 degrees and each star is mapped to a simulated SkyHopper focal plane. The AB magnitude of each star is corrected and converted to photon flux densities. Fluxes from z' band at 9134Å and i' band at 7625Å are averaged to approximate the strength of an object's continuum near the calcium triplet absorption feature at $\sim$ 8500Å.

Figure 4.6 shows the resulting mock images of a portion of the NEP field using a Gaussian PSF of FWHM ranging from 1 arcseconds to 5 arcseconds. The impact of PSF size is apparent, though it is noted these mock images do not contain noise or a sky background of any level.

By taking the difference of the two images in the OFF and ON narrowbands the overall calcium absorption feature from the Zodiacal light can be measured. To determine the noise contribution, a Zodiacal light level of $\sim 7.36 \times 10^{-7}\ photon/cm^2/s/\text{Å}/arcsec^2$ is added uniformly to the mock pixels shown in figure 4.6 with an appropriate scaling for the absorption feature present just in the ON filter. Noise was then added using the baseline parameters defined in section 4.5. The total exposure time is taken to be the maximum for the NEP field of 588 minutes, with optimal sub exposure time of 36 minutes (i.e. one exposure per orbit).

The resulting pixel values in instrumental counts of e^-/pix are shown in figure 4.7a for varying PSF FWHM from 1 arcseconds to 5 arcseconds in the ON and OFF narrow band fields. The difference of the two distributions are shown in figure 4.7. The mean is found to vary only slight with respect to increasing PSF FWHM. The errors on the means for 1 and 5 arcsecond PSF FWHM are found using a bootstrap re-sampling method. The corresponding SNR is $\sim$ 600 and $\sim$ 300, respectively. While these SNR values are smaller than that estimated in section 4.5, it is noted the analysis did not include any optimisation from masking pixels with bright sources. So while future work on this is needed, this initial quick analysis indicates a large portion of the pixels may be used to obtain a robust Zodiacal light measure, even if the PSF sizes are large. As a result this would reduce the pixel masking fraction needed for narrowband Zodiacal light measurements, possibly increasing the achievable SNR.

4.7 Results

As a result of the work presented in this chapter, the maximum exposure time for narrow band observations is found to be restricted by the rapid change in Zodiacal light intensity depending upon the ecliptic latitude of the field. The NEP field has the highest total exposure time at 588 minutes, followed by the SWIRE field at 106 minutes, and finally the BOOTES

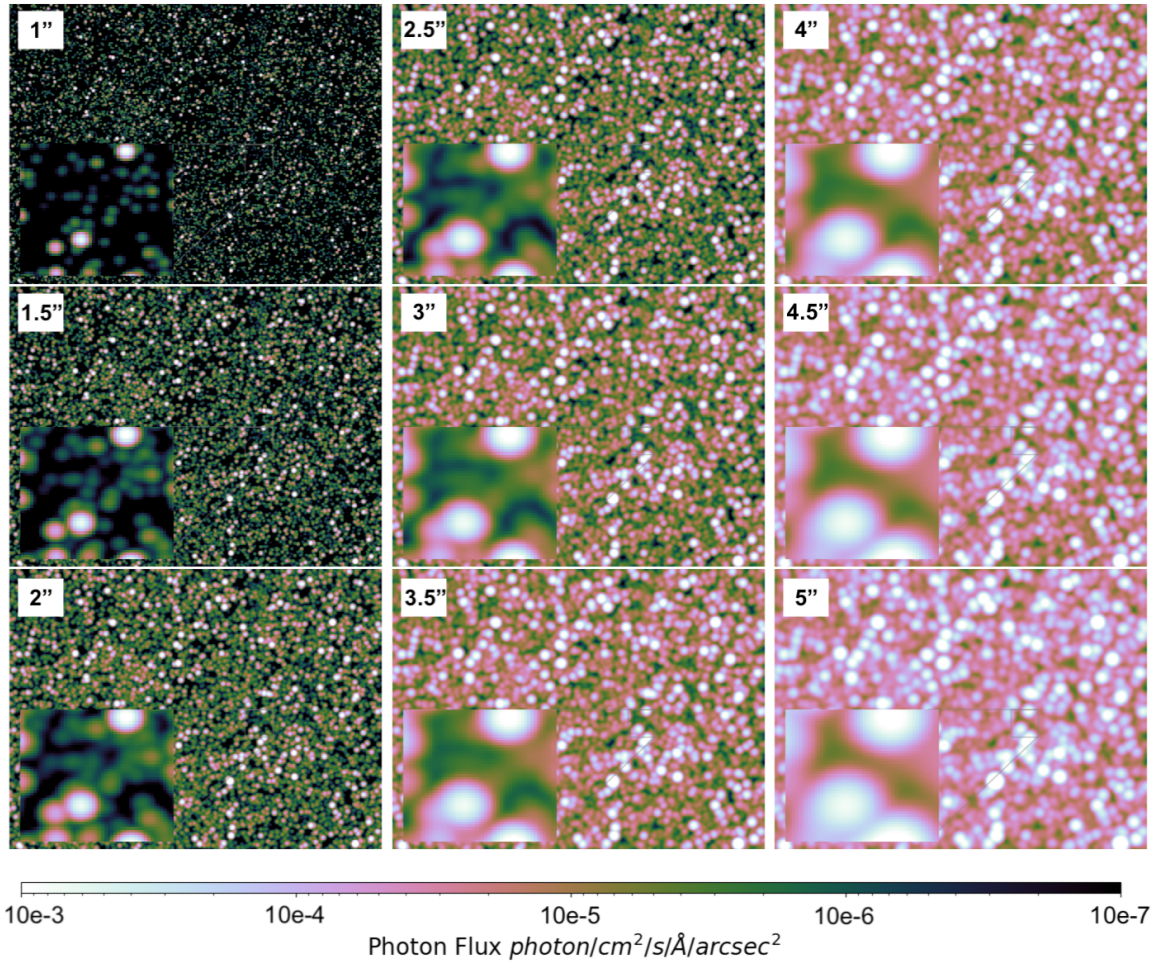

Figure 4.6: Mock images for a SkyHopper narrowband filter before addition of noise using SDSS corrected photon flux densities for varying PSF widths in the NEP field. Only a 0.76×0.57 deg^2 portion of the NEP field is shown. Source location and brightness are estimate of the continuum near $\sim$ 8500Å from $i-$ and $z-$band SDSS data. No sky background is included. For reference the Zodiacal light strength is $\sim 7.36e^{-7}$ $photon/cm^2/s/\text{Å}/arcsecond^2$

fields at 88 minutes before Zodiacal light intensity changes by more than 0.1%.

Modelling of SkyHoppers visibility for the chosen fields shows that the visibility over the course of the first year of operations for the NEP and SWIRE fields are not impacted by the pointing constraints derived in chapter 3. The BOOTES field is impacted due to its lower ecliptic latitude and its best observation period is between January and July when Zodiacal light intensity is the lowest.

A robust Bayesian SkyHopper model (see Figure A.1 for more examples) is constructed to explore SkyHopper mission requirements. The result of exposure time calculations show that the most important factor in determining the SNR achieved is the read noise of the detector. For the SNR goal of 1000 for the Zodiacal light, it appears the 36 minutes sub exposures are important for the BOOTES and SWIRE fields, but less so for the NEP because we have a larger amount of time (588 minutes) to constrain the Zodiacal light levels before they change. If read noise is restricted to no more than 12.5 e^-/pix, all fields reach the goal defined SNR of 1000. Dark current is found to have a negligible impact on the SNR of observations within the maximum and goal defined operating limits of the manufacturer.

An initial study into the impact of bright sources in mock SkyHopper images with

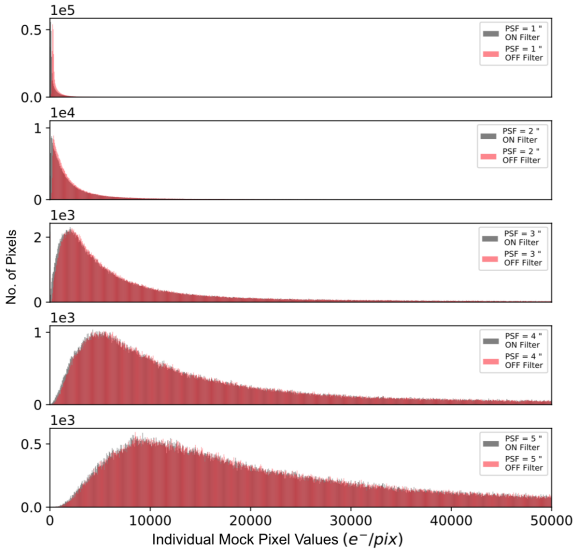

(a)

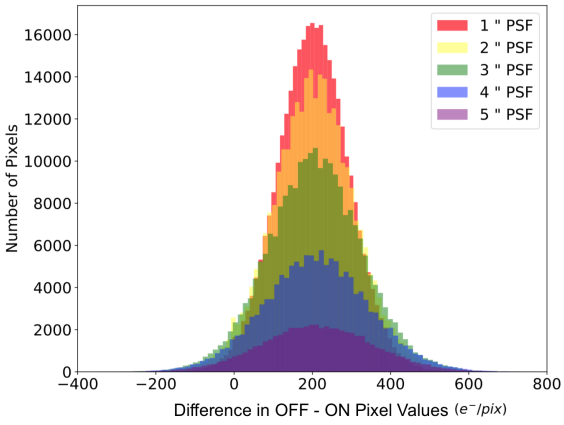

(b)

Figure 4.7: These figures illustrate how individual pixels that have some stellar light can still contribute meaningfully to the Zodiacal light measurement. For these plots, realistic noise was introduced and is reflected in the pixel values. *LEFT*: Distributions of individual pixel values for various PSF FWHMs in the ON (grey) and OFF (red) band filters (see section 2.3). The distribution of the signal is spread out to higher instrumental fluxes as the PSF is increased and more pixels are contaminated by bright sources. The slight shift in pixel values from the ON filter reflects the fact that it is centred on the strong calcium triplet absorption feature. *RIGHT*: Pixel values after subtraction of the OFF and ON band images for different PSF FWHM. The non-zero difference indicates the Zodical light level is recoverable, even for a fairly large FWHM of 5 arcseconds.

increased PSF width indicates that it may be possible to use use a larger fraction of pixels for narrowband Zodiacal light observations. Further work is needed translate these results into an achievable pixel masking fraction for future exposure time calculations.

5 Future Work

5.1 Measuring Zodiacal Light with Hubble Ramp Filters

Measurement of the COIB has been attempted in the past with the Hubble Space Telescope [Bernstein, 2007], as discussed in chapter 1. This result was found to be significantly impacted by uncertainties in the measurement of the Zodiacal light intensity simultaneously from the ground at the same time that Hubble measurements of the COIB were being taken [Mattila, 2003]. During the preparation of this thesis, I explored the possibility of conducting a pure parallel program with Hubble to measure the COIB. This included measuring the Zodiacal light intensity with a narrowband ramp filter on Hubble to avoid the uncertainties present in measurements conducted by Bernstein [2007].

Preliminary work into this idea looks promising. The design and implementation of pure parallel program for cycle 28 is anticipated to form part of my PhD, as a complementary work along side the SkyHopper COIB science case. The initial description of the program as described below.

Hubble has no dedicated calcium triplet narrow band filters to constrain the Zodiacal light directly. Hubble's ACS camera has a tunable ramp filter, FR853N, that can be centered on any wavelength between 8158Å - 8905Å and will be used to measure the strength of the Zodiacal light in a similar way to the SkyHopper method outlined in section 2.3. In order to measure the COIB light in broader bandwidth filters, we will also make use of the F435W, F606W, F814W and F850LP filters. The Zodiacal light constraint plus an assumed Zodiacal light SED will be used to subtract an estimate of the Zodiacal light from the broadband filters. If appropriate Earthshine constraints are included, after the Zodiacal light is removed only a COIB component will remain in the broadband filter data.

During this thesis, I built a custom Hubble instrument model using `PySynphot` as a guide. The aim is to build upon this model in a similar way to the SkyHopper model presented in chapter 4 to constrain systematic uncertainties in the measurement.

5.2 Complete Mock SkyHopper Observations

My work on the COIB science case has only focused on successful detection and subtraction of the Zodiacal light foreground using the SkyHopper narrowband filters. The next step is to build in upper and lower limits of COIB intensity and the impact of galactic cirrus into the Bayesian instrument model constructed as part of this thesis. I aim to complete this analysis of the science requirements before the commencement of my PhD in 2020 with the goal of feeding them into the overall SkyHopper mission requirements.

I also plan to investigate other forms of systematic error that may be an issue to SkyHopper. The production of Cherenkov radiation in the Kestors prism as a result of high energy charged particles slowing down in the glass is also of particular concern as a systematic uncertainty.

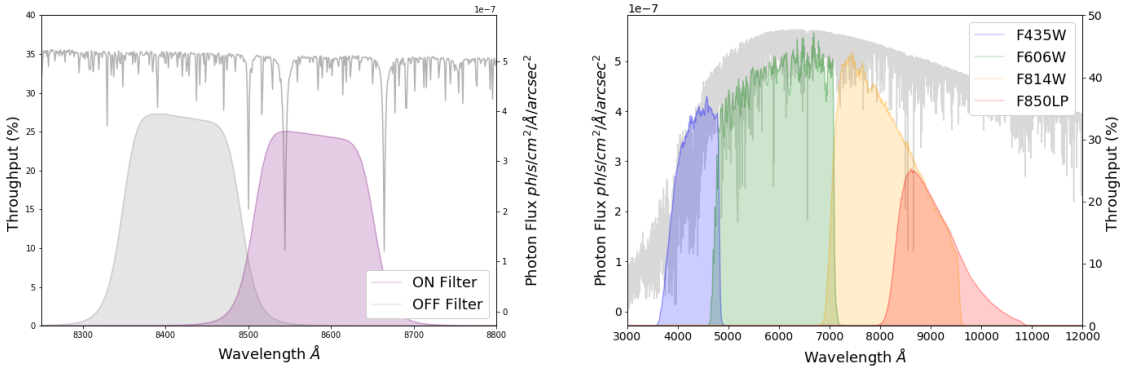

Figure 5.1: LEFT: Hubble narrow band ramp filter placement for measurement of the strength of the calcium triplet absorption feature. RIGHT: Broad band filters selected to make measurements of the COIB in optical to near infrared wavelengths after Zodiacal light subtraction.

An initial investigation into the impact of Cherenkov radiation on the Australian Space Eye concept was explored by University of Wollongong masters student Alex Augustine [Augustine, 2017]. Augustine concludes that due to the non uniform distribution of electrons in the Earth's magnetosphere, polar orbits suffer higher intensity radiation due to Cherenkov as compared to equatorial orbits. Further work is needed to assess the impact of Cherenkov radiation on observations and possibly motivate radiation shielding of the instrument.

6
Conclusions

As part of the work presented in this thesis, I have created a new algorithm to quantify the Earthshine beneath a space telescope with the use of NASA CERES satellite weather data. Development is underway for the release of this algorithm as an open source Python package which can be used by any space telescope project.

In chapter 3, I identify the orbital parameters that are most important in avoiding the impact of Earthshine for the COIB science case by using archived Hubble sky background data and collated information about the pointing of the instrument. I present an analysis of the impact of Sun altitude and limb angle on the background of Hubble observations, and determine that these quantities must have constraints placed on them for successful avoidance of Earthshine. I show that the standard deviation of background observed by Hubble can be reduced by as much as $\sim$ 50% and a reduction in the mean background sky observed by $\sim$ 14% by limiting the Sun altitude of the telescope to 0 degrees, and ensuring the limb angle of an observation is no less than 35 degrees. These findings suggest we can simply place the constraints on these orbital parameters and ensure SkyHopper completely avoids contamination from Earthshine.

In chapter 3, I identify a possible disagreement between observations and theoretical models of Zodiacal light intensity. By investigating the temporal variation in observed sky background in Hubble fields, I find a discrepancy as high as 8.91%. This level of uncertainty means we cannot use existing models of Zodiacal light and instead must measure Zodiacal light intensity directly with SkyHopper to perform an accurate subtraction from the COIB data.

In chapter 4, I construct a SkyHopper optical payload model with the `PyMC3` Bayesian framework in order to produce a robust and modular exposure time calculator. This model will form the basis of a larger model that will be used to perform Bayesian inference on SkyHopper COIB observations. This will also allow for an accurate propagation of systematic uncertainties in the final measurement.

I identify the maximum exposure time of SkyHopper narrowband observations that can be used to constrain Zodiacal light intensity variation to less than 0.1%. I also identify the best windows of observation for each SkyHopper COIB field by calculating the visibility of SkyHopper fields given the orbital constraints presented above in order to successfully constrain Zodiacal light intensity. The NEP field is identified to have the highest maximum allowed exposure time of 588 minutes followed by the SWIRE field at 106 minutes. The field with the lowest total exposure time is the BOOTES field with 88 minutes. The goal defined SNR of 1000 is reached by all fields, provided a minimum sub exposure time of 36 minutes is reached.

The results of initial exposure time calculations indicate that the parameter that has the highest influence on the signal to noise for all fields is the read noise. In order to reach the

target accuracy across all fields of 0.1% for narrowband observations, a read noise less than $12.5 e^{-}/pix$ is needed. This read noise is within manufacture quoted specifications with a sampling up the ramp (SUTR) readout mode and frame rate of $\sim$ 13 per exposure. Dark current within the total range quoted by the manufacturer is found to have little impact on the achieved SNR.

The result of these findings motivate the decision to use SUTR as preferred readout mode for SkyHopper COIB observations. SUTR produces a low readout noise which can be further reduced with an increase frame rate. Not only does this reduce the total read noise, but as presented in the literature, it also has the potential to reduce the impact of cosmic rays and reduce the impact of bright sources in the field of view.

I conduct preliminary investigations into the development of mock images for SkyHopper observations to explore the impact of an increase PSF width. While future work is needed, this initial step indicates that it may be possible to use a larger portion of pixels in the image to obtain a robust measurement of Zodiacal light intensity, even with larger PSF widths.
As a result of the work presented in this thesis, the following has been achieved:

1. The development of a novel method of quantifying Earthshine beneath a space telescope that has provided initial SkyHopper pointing constraints for the COIB science case.

2. The design of an observing program with SkyHopper to accurately detect and subtract the Zodiacal light foreground emission. Further work is anticipated in the following months as the science payload and spacecraft design details are constrained by the SkyHopper consortium.

3. The construction of a Bayesian instrument model to simulate the performance of the instrument and produce initial systematic error analysis that will be extended for the anticipated COIB measurement.

6.1 What is Next for SkyHopper?

The SkyHopper project is now on track to deliver SkyHopper to orbit by the end of 2022 to 2023. The SkyHopper consortium continues to grow, with representation from collaborating universities around Australia, the United States and Europe.

The findings of this thesis represent only the first steps toward deriving the science requirements of the COIB science case. In future work and my PhD, I look forward to continue collaborating with the SkyHopper team and hope to see the impact of the mission in inspiring the next generation of space based observatories developed in Australia.

In the future, maybe we will see a small, shoebox-sized space telescope make a measurement of the light from the first galaxies that existed in our Universe.

A Appendix

A.1 Software

The work in this thesis has made substantial use of the following Python libraries:

Gunagala: https://gunagala.readthedocs.io/en/develop/index.html
PyMC3: https://docs.pymc.io/
Astropy: https://www.astropy.org/
SciPy: https://www.scipy.org/
PySynPhot: https://pysynphot.readthedocs.io/en/latest/
PyEphem: https://pypi.org/project/ephem/
Matplotlib: https://matplotlib.org/
netCDF4: https://pypi.org/project/netCDF4/
NumPy: https://numpy.org/
Pandas: https://pandas.pydata.org/

A.2 Supplemental Material

SED Source	Normalisation	Details
Zodiacal Light	High: $4.75e^{-18} erg/s/cm^2/A/arcsec^2$ Mid: $3.00e^{-18} erg/s/cm^2/A/arcsec^2$ Low: $1.72e^{-18} erg/s/cm^2/A/arcsec^2$ [Giavalisco, 2002]	Blue reddening parameter of 0.9 Red parameter of 0.48 V band flux norm: $184.2\, ergs/s/cm^2/A$
Earthshine	Average: $\sim 1.00e^{-18} erg/s/cm^2/A/arcsec^2$ Upper Limit: $\sim 6.00e^{-18} erg/s/cm^2/A/arcsec^2$ [Giavalisco, 2002]	Air mass zero American society for testing mater E-490 reference spectra
COIB	Upper limit: [Dwek and Krennrich, 2013] Lower limit: [Driver et al., 2016]	Upper limit: Interpolated COBE, DIRBE data Lower limit: Integrated galaxy counts

Table A.1: Details of the normalisation parameters and references for the modeled SEDs used in this work and the python packages constructed during this thesis.

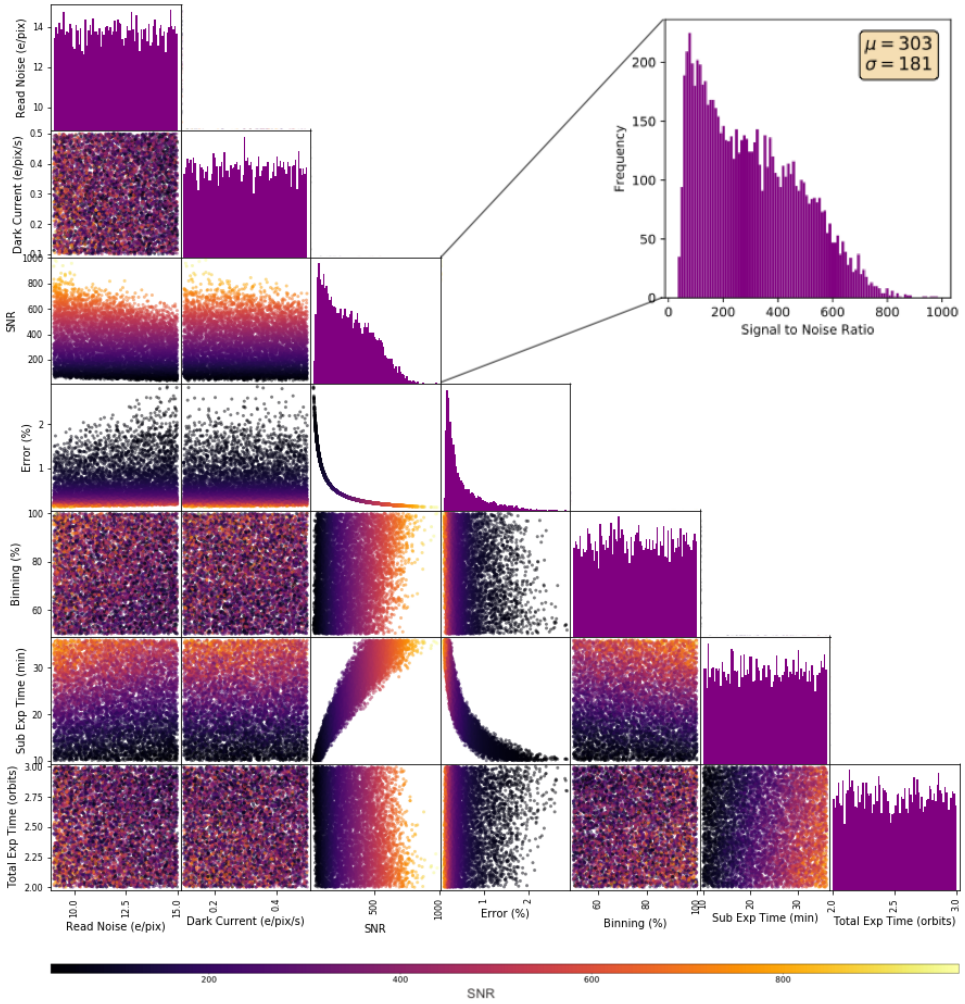

Figure A.1: By implementing complex models in a *PyMC3* framework that uses MCMC sampling I can also explore a large unconstrained parameter space. This figure is based on a simpler model compared to chapter 4, where I assume uniform, uninformed priors within reasonable bounds for an observation. Bounds for each prior are shown in the axes for each plot. In this way, the entire SNR distribution is produced for every possible combination of instrument parameters. While this analysis cannot be used in Bayesian inference for SkyHopper observation like the model produced in chapter 4, it can be used as a quick diagnostic tool, to explore the impact of constrained parameters on the SNR.

Parameter	Goal	Average
Dark Current (median)	$\leq 0.01\, e^-/s$	$\leq 0.05\, e^-/s$
Read Noise (median) CDS at 100kHz	$\leq 15\, e^-$	$\leq 30\, e^-$
QE at 800nm	$\geq 70\%$	$\geq 50\%$
QE at 1000nm	$\geq 70\%$	$\geq 50\%$
QE at 1230nm	$\geq 80\%$	$\geq 70\%$
QE at 1500nm	$\geq 80\%$	$\geq 70\%$

Table A.2: The goal and average detector performance for SkyHoppers HAWAII-2RG detector. The SkyHopper instrument model assumes goal defined detector parameters unless otherwise stated. For further details of the HAWAII-2RG detector please see [Teledyne].

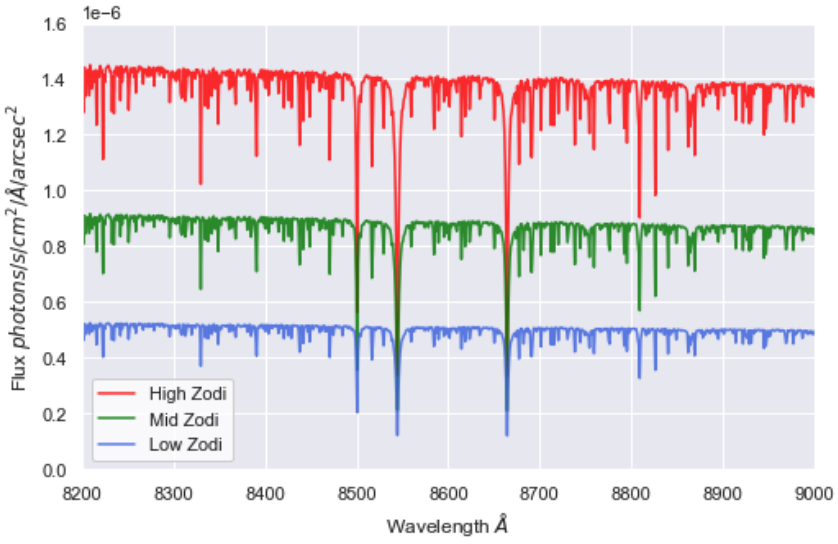

Figure A.2: High (red), medium (green) and low (blue) Zodiacal light (zodi) normalisation for reference based upon the work of Giavalisco [2002]. Presented SEDs are in units of $photon/s/cm^2/\text{Å}/arcsec^2$ and centered on the calcium triplet absorption features.

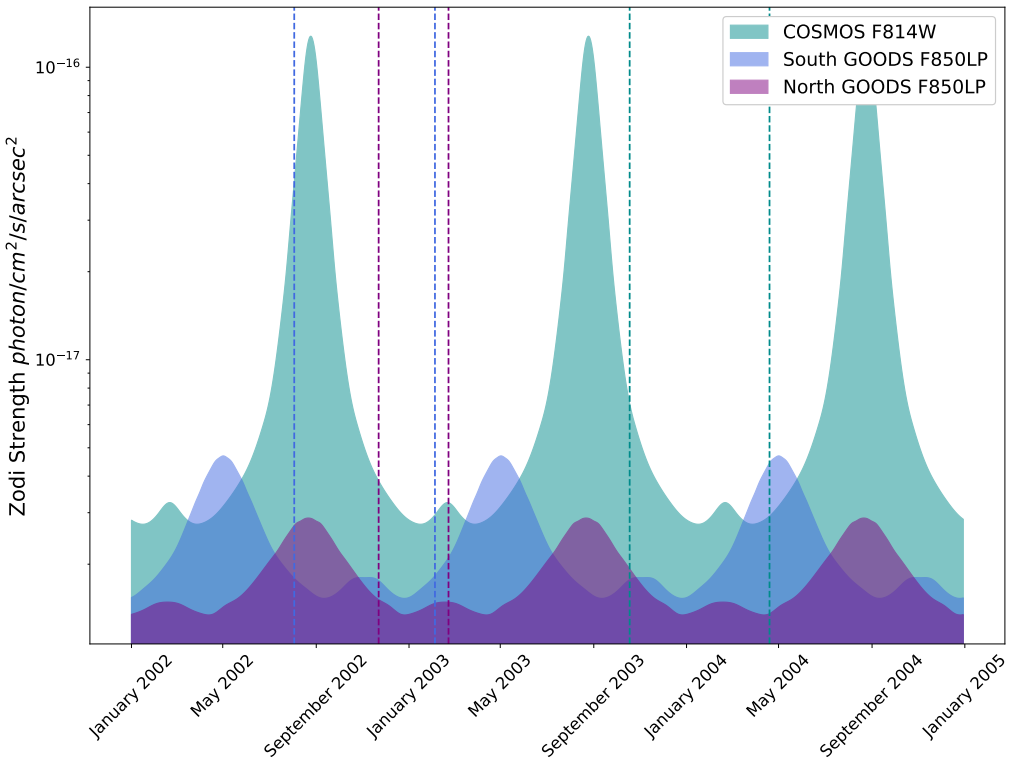

Figure A.3: Variation in intensity of Zodiacal light for North and South GOODS fields, and the COSMOS field from January 2002 to December 2004 over the period observations were taken. Dotted lines indicate the date of the observations used in this study.

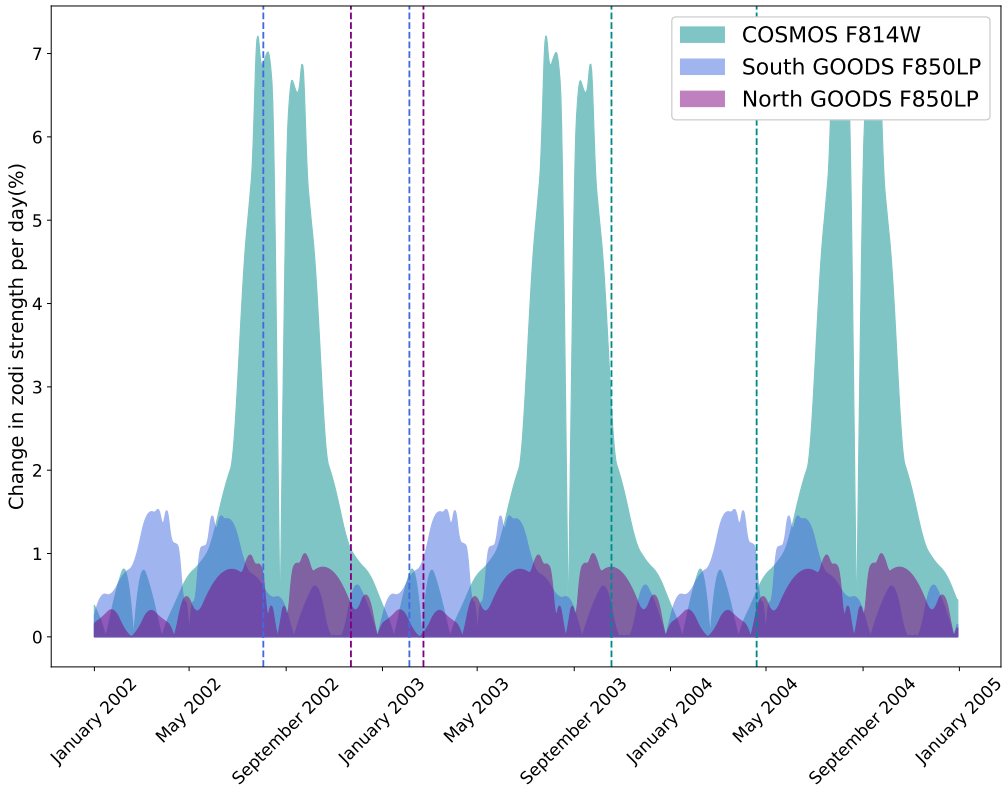

Figure A.4: The derived percentage change in zodiacal light intensity per day for North and South GOODS fields, and the COSMOS field from January 2002 to December 2004. Dotted lines indicate the date of the observations used in this study.

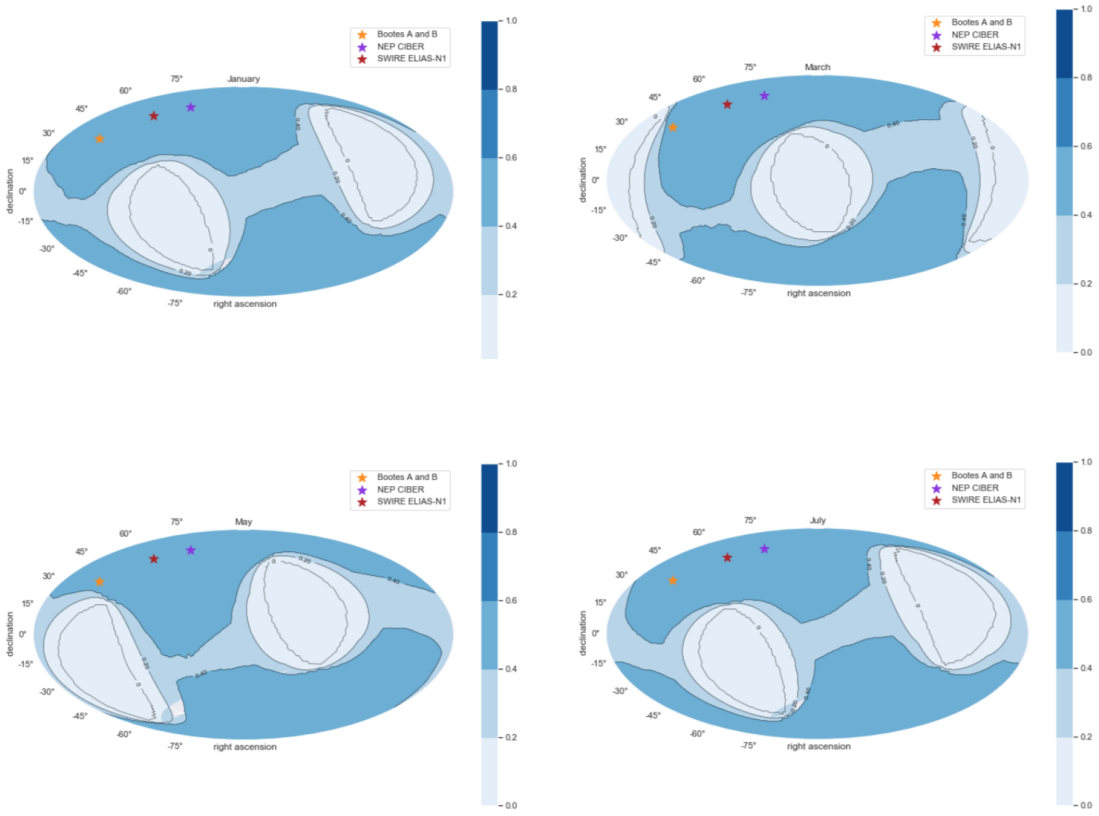

Figure A.5: A static example of the field visibility plots for SkyHopper. Location of the fields are plotted in equatorial coordinates. Shading indicates the fraction of visibility of the field given the pointing constraints derived in Chapter 3.

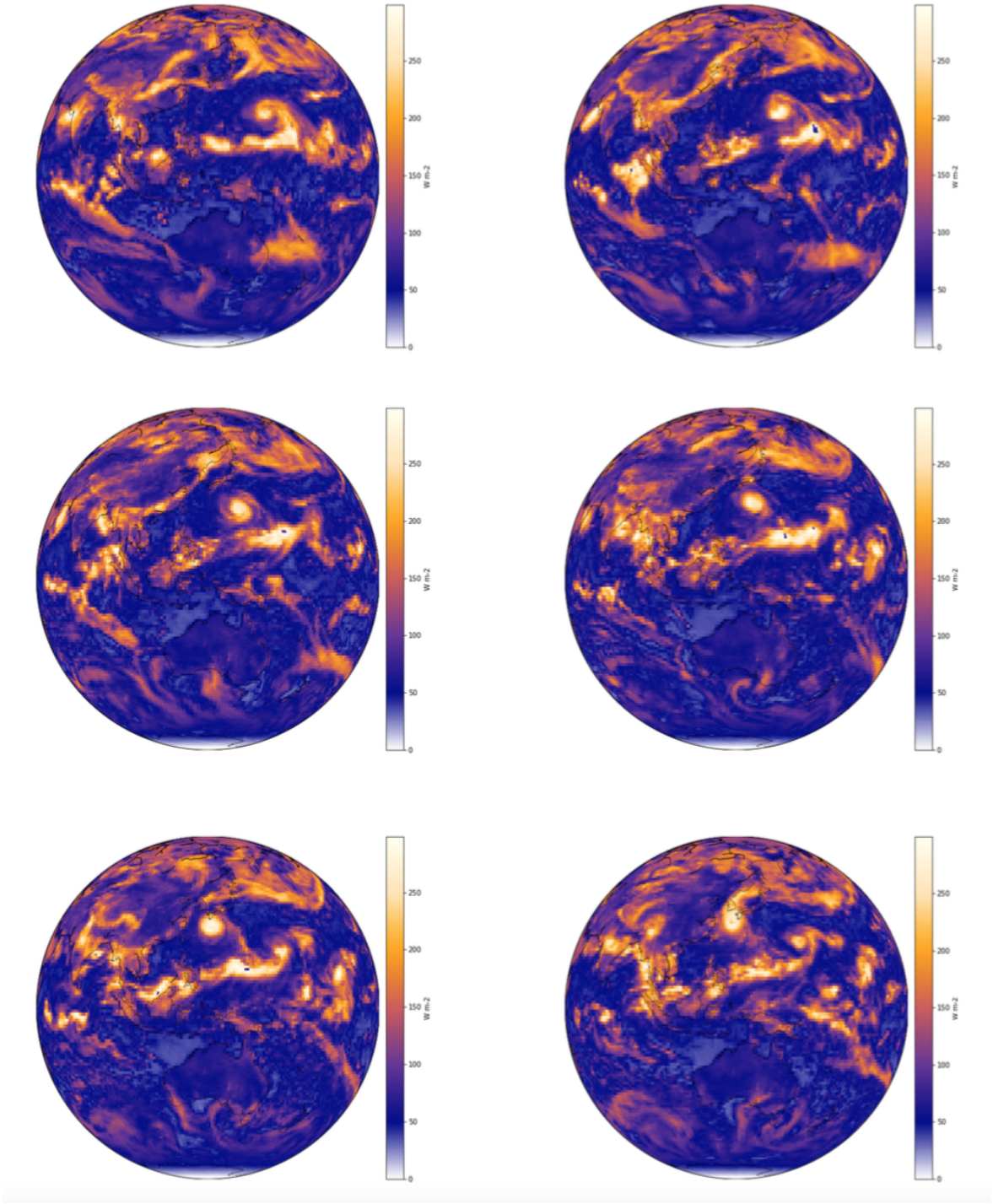

Figure A.6: A static example of the variation in upwards flux as seen by CERES from the top of the atmosphere over a period of 6 days over Australia. Shading is the intensity of the upward flux in W/m^2.

References

T. Arai, S. Matsuura, J. Bock, A. Cooray, M. G. Kim, A. Lanz, D. H. Lee, H. M. Lee, K. Sano, J. Smidt, T. Matsumoto, T. Nakagawa, Y. Onishi, P. Korngut, M. Shirahata, K. Tsumura, and M. Zemcov. Measurements of the mean diffuse Galactic light spectrum in the 0.95-1.65 μm band from CIBER. *Astrophysical Journal*, 806(1), 6 2015. ISSN 15384357. doi: 10.1088/0004-637X/806/1/69.

A. Augustine. Modelling of Light Sources for Optimal Astronomy Imaging Analysis. Master's thesis, University of Wollongong, 2017.

W. Ballhaus, J. Casani, S. Dorfman, D. Gallagher, K. Swales, D. Schurr, and R. Lewis. James Webb Space Telescope (JWST) Independent Comprehensive Review Panel (ICRP) final report. Technical report, 2010.

J. Beletic. IR focal-plane arrays enabling imaging that is out of this world. *Laser Focus World*, pages 75–58, 10 2007.

D. J. Benford, T. R. Lauer, and D. B. Mott. Simulations of sample-up-the-ramp for space-based observations of faint sources. In D. A. Dorn and A. D. Holland, editors, *High Energy, Optical, and Infrared Detectors for Astronomy III*, volume 7021, page 70211V. SPIE, 8 2008. doi: 10.1117/12.789976.

R. A. Bernstein. The optical extragalactic background light: revisions and further comments. *The Astrophysical Journal*, 666:663–673, 2007.

R. A. Bernstein, W. L. Freedman, and B. F. Madore. The first detections of the extragalactic background light at 3000, 5500, and 8000 results. *The Astrophysical Journal*, 571:56–84, 2002.

H. Bethermin, M. Dole. Measurements of the spectral energy distribution of the cosmic infrared background. page 002, 05 2011. doi: 10.22323/1.121.0002.

J. Biretta, D. Van Orsow, W. Sparks, M. Reinhart, and A. Vick. ACS Background Light vs. Bright Earth Limb Angle. Technical report, 2003.

J. Bock, J. Battle, A. Cooray, M. Kawada, B. Keating, A. Lange, D.-H. Lee, T. Matsumoto, S. Matsuura, S. Pak, T. Renbarger, I. Sullivan, K. Tsumura, T. Wada, and T. Watabe. The cosmic infrared background experiment. *New Astronomy Reviews*, 50(1-3):215–220, 3 2006. ISSN 13876473. doi: 10.1016/j.newar.2005.11.034.

S. P. Boughn and J. R. Kuhn. The search for extragalactic background light using the dark cloud L134. *The Astrophysical Journal*, 309:33–38, 1986. doi: 10.1086/164574.

R. J. Bouwens, G. D. Illingworth, P. A. Oesch, M. Stiavelli, P. van Dokkum, M. Trenti, D. Magee, I. Labbe, M. Franx, M. Carollo, and V. Gonzalez. Discovery of z = 8 Galaxies in the HUDF from ultra deep WFC3/IR Observations. *The Astrophysical Journal Letters, Volume 709, Issue 2, pp. L133-L137 (2010).*, 709:L133–L137, 9 2009. ISSN 0004-637X. doi: 10.1088/2041-8205/709/2/L133.

A. Cooray. Extragalactic background light measurements and applications. *Royal Society Open Science*, 3(150555), 2016. doi: 10.1098/rsos.150555.

R. Diaz. Zodiacal Light contribution for the UV ETC background. Technical report, Space Telescope Science Institute, 2015.

S. P. Driver, S. K. Andrews, L. J. Davies, A. S. G. Robotham, A. H. Wright, R. A. Windhorst, S. Cohen, K. Emig, R. A. Jansen, and L. Dunne. Measurements of extragalactic background light from the far UV to the far IR from deep ground-and space-based galaxy counts. 2016. doi: 10.3847/0004-637X/827/2/108.

E. Dwek and F. Krennrich. The extragalactic background light and the gamma-ray opacity of the universe. *Astroparticle Physics*, 43:112–133, 2013. doi: 10.1016/j.astropartphys.2012.09.003.

P. R. Eisenhardt, D. Stern, M. Brodwin, G. G. Fazio, G. H. Rieke, M. J. Rieke, M. W. Werner, E. L. Wright, L. E. Allen, R. G. Arendt, M. L. N. Ashby, P. Barmby, W. J. Forrest, J. L. Hora, J.-S. Huang, J. Huchra, M. A. Pahre, J. L. Pipher, W. T. Reach, H. A. Smith, J. R. Stauffer, Z. Wang, S. P. Willner, M. J. I. Brown, A. Dey, B. T. Jannuzi, and G. P. Tiede. The IRAC Shallow Survey. 2004.

G. Finger, R. J. Dorn, M. Meyer, L. Mehrgan, J. Stegmeier, and A. F. M. Moorwood. Performance of large format 2Kx2K MBE grown HgCdTe Hawaii-2RG arrays for low flux applications. Technical report, 2004.

A. Fruchter and M. Sosey. The MultiDrizzle Handbook A Guide for Combining HST Images. Technical report, Space Telescope Science Institute, Baltimore, Maryland 21218, 2009.

J. P. Gardner, J. C. Mather, M. Clampin, R. Doyon, M. A. Greenhouse, H. B. Hammel, J. B. Hutchings, P. Jakobsen, S. J. Lilly, K. S. Long, J. I. Lunine, M. J. Mccaughrean, M. Mountain, J. Nella, G. H. Rieke, M. J. Rieke, H.-W. Rix, E. P. Smith, G. Sonneborn, M. Stiavelli, H. S. Stockman, R. A. Windhorst, and G. S. Wright. The James Webb Space Telescope. *Space Science Reviews*, 123(4):485–606, 11 2006. ISSN 0038-6308. doi: 10.1007/s11214-006-8315-7.

M. Giavalisco. Lyman-Break Galaxies. *Annu. Rev. Astron. Astrophys*, 40:579–641, 2002. doi: 10.1146/annurev.astro.40.121301.111837.

M. Giavalisco, K. Sahu, and R. C. Bohlin. New Estimates of the Sky Background for the HST Exposure Time Calculator. Technical report, 2002.

M. Giavalisco, H. C. Ferguson, A. M. Koekemoer, M. Dickinson, D. M. Alexander, F. E. Bauer, J. Bergeron, C. Biagetti, W. N. Brandt, S. Casertano, C. Cesarsky, E. Chatzichristou, C. Conselice, S. Cristiani, L. Da Costa, T. Dahlen, D. de Mello, P. Eisenhardt, T. Erben, S. M. Fall, C. Fassnacht, R. Fosbury, A. Fruchter, J. P. Gardner, N. Grogin, R. N. Hook, A. E. Hornschemeier, R. Idzi, S. Jogee, C. Kretchmer, V. Laidler, K. S. Lee, M. Livio, R. Lucas, P. Madau, B. Mobasher, L. A. Moustakas, M. Nonino, P. Padovani, C. Papovich, Y. Park, S. Ravindranath, A. Renzini, M. Richardson, A. Riess, P. Rosati, M. Schirmer, E. Schreier, R. S. Somerville, H. Spinrad, D. Stern, M. Stiavelli, L. Strolger, C. M. Urry, B. Vandame, R. Williams, and C. Wolf. The Great Observatories Origins Deep Survey: Initial Results from Optical and Near-Infrared Imaging. *The Astrophysical Journal*, 600 (2):L93–L98, 1 2004. ISSN 0004-637X. doi: 10.1086/379232.

W. Hack, N. Dencheva, C. Sontag, M. Sosey, M. Droettboom, and M. Cara. DrizzlePac Documentation. Technical report, 2019. URL https://buildmedia.readthedocs.org/media/pdf/drizzlepac/deployment/drizzlepac.pdf.

M. G. Hauser and E. Dwek. The Cosmic Infrared Background: Measurements and Implications. *Annual Review of Astronomy and Astrophysics*, 39(1):249–307, 9 2001. doi: 10.1146/annurev.astro.39.1.249.

R. Hill, K. W. Masui, and D. Scott. The Spectrum of the Universe. *Applied Spectroscopy*, 72(5):663–688, 5 2018. ISSN 0003-7028. doi: 10.1177/0003702818767133.

A. Horton, L. Spitler, N. Mathers, M. Petkovic, D. Griffin, S. Barraclough, C. Benson, I. Dimitrijevic, A. Lambert, A. Previte, J. Bowen, S. Westerman, J. Puig-Suari, S. Reisenfeld, J. Lawrence, R. Zhelem, M. Colless, and R. Boyce. The Australian Space Eye: studying the history of galaxy formation with a CubeSat. 6 2016. doi: 10.1117/12.2232467.

A. M. Koekemoer, H. Aussel, D. Calzetti, P. Capak, M. Giavalisco, J. Kneib, A. Leauthaud, O. Le Fevre, H. J. McCracken, R. Massey, B. Mobasher, J. Rhodes, N. Scoville, and P. L. Shopbell. The COSMOS Survey: Hubble Space Telescope Advanced Camera for Surveys Observations and Data Processing . *The Astrophysical Journal Supplement Series*, 172(1): 196–202, 9 2007. ISSN 0067-0049. doi: 10.1086/520086.

P. M. Korngut, T. Renbarger, T. Arai, J. Battle, J. Bock, S. W. Brown, A. Cooray, V. Hristov, B. Keating, M. G. Kim, A. Lanz, D. H. Lee, L. R. Levenson, K. R. Lykke, P. Mason, T. Matsumoto, S. Matsuura, U. W. Nam, B. Shultz, A. W. Smith, I. Sullivan, K. Tsumura, T. Wada, and M. Zemcov. The cosmic infrared background experiment (CIBER): The narrow-band spectrometer. *Astrophysical Journal, Supplement Series*, 207(2), aug 2013. ISSN 00670049. doi: 10.1088/0067-0049/207/2/34.

J. E. Krick, W. J. Glaccum, S. J. Carey, P. J. Lowrance, J. A. Surace, J. G. Ingalls, J. L. Hora, and W. T. Reach. A Spitzer/IRAC measure of the zodiacal light. *Astrophysical Journal*, 754(1), 2012. ISSN 15384357. doi: 10.1088/0004-637X/754/1/53.

D. Leob and E. Kizer. Clouds and the Earth's Radiant Energy System (CERES), 2019. URL https://ceres.larc.nasa.gov/.

N. G. Loeb, D. R. Doelling, H. Wang, W. Su, C. Nguyen, J. G. Corbett, L. Liang, C. Mitrescu, F. G. Rose, S. Kato, N. G. Loeb, D. R. Doelling, H. Wang, W. Su, C. Nguyen, J. G. Corbett, L. Liang, C. Mitrescu, F. G. Rose, and S. Kato. Clouds and the Earth's Radiant Energy System (CERES) Energy Balanced and Filled (EBAF) Top-of-Atmosphere (TOA) Edition-4.0 Data Product. *Journal of Climate*, 31(2):895–918, 1 2018. ISSN 0894-8755. doi: 10.1175/JCLI-D-17-0208.1.

C. J. Lonsdale, H. E. Smith, M. Rowan Robinson, J. Surace, D. Shupe, C. Xu, S. Oliver, D. Padgett, F. Fang, T. Conrow, A. Franceschini, N. Gautier, M. Griffin, P. Hacking, F. Masci, G. Morrison, J. OLinger, F. Owen, I. Perez Fournon, M. Pierre, R. Puetter, G. Stacey, S. Castro, M. Del Carmen Polletta, D. Farrah, T. Jarrett, D. Frayer, B. Siana, T. Babbedge, S. Dye, M. Fox, E. Gonzalez Solares, M. Salaman, S. Berta, J. J. Condon, H. Dole, and S. Serjeant. SWIRE: The SIRTF Wide Area Infrared Extragalactic Survey. *Publications of the Astronomical Society of the Pacific*, 115(810):897–927, 8 2003. doi: 10.1086/376850.

M. Loose, J. Beletic, J. Garnett, and M. Xu. High-Performance Focal Plane Arrays Based on the HAWAII-2RG/4RG and the SIDECAR ASIC. 2010. doi: 10.1117/12.735625.

H. Matsuhara, T. Wada, S. Matsuura, T. Nakagawa, M. Kawada, Y. Ohyama, C. P. Pearson, S. Oyabu, T. Takagi, S. Serjeant, G. J. White, H. Hanami, H. Watarai, T. T. Takeuchi, T. Kodama, N. Arimoto, S. Okamura, H. Mok Lee, S. Pak, M. Shin Im, M. Gyoon Lee, W. Kim, W.-S. Jeong, K. Imai, N. Fujishiro, M. Shirahata, T. Suzuki, C. Ihara, and I. Sakon. Deep Extragalactic Surveys around the Ecliptic Poles with AKARI (ASTRO-F). Technical report, 2006.

Y. Matsuoka, N. Ienaka, K. Kawara, and S. Oyabu. Cosmic optical background: the view from pioneer 10/11. *The Astrophysical Journal*, 736(14pp):119, 2011. doi: 10.1088/0004-637X/736/2/119.

S. Matsuura, T. Arai, J. J. Bock, A. Cooray, P. M. Korngut, M. G. Kim, H. M. Lee, D. H. Lee, L. R. Levenson, T. Matsumoto, Y. Onishi, M. Shirahata, K. Tsumura, T. Wada, and M. Zemcov. New Spectral Evidence of an Unaccounted Component of the Near-infrared Extragalactic Background Light from the CIBER . *The Astrophysical Journal*, 839(1):7, apr 2017. ISSN 1538-4357. doi: 10.3847/1538-4357/aa6843.

K. Mattila. On the measurement of the extragalactic background brightness at 4000 A. *Astronomy and Astrophysics*, 47:77–95, 1976.

K. Mattila. Observations of the extragalactic background light. Technical report, IAU Symposium, 1990.

K. Mattila. Comments on "The first detections of the Extragalactic Background Light at 3000, 5500, and 8000 A" by Bernstein, Freedman and Madore. *The Astrophysical Journal, Volume 591, Issue 1, pp. 119-124.*, 591:119–124, 3 2003. ISSN 0004-637X. doi: 10.1086/375182.

K. Mattila and P. Väisänen. Extragalactic background light: inventory of light throughout the cosmic history. *Contemporary Physics*, pages 1–22, 3 2019. ISSN 0010-7514. doi: 10.1080/00107514.2019.1586130.

K. Mattila, P. Väisänen, K. Lehtinen, G. von Appen-Schnur, and C. Leinert. Extragalactic background light: A measurement at 400 nm using dark cloud shadow - II. Spectroscopic separation of the dark cloud's light, and results. *Monthly Notices of the Royal Astronomical Society*, 470(2):2152–2169, 9 2017. ISSN 13652966. doi: 10.1093/mnras/stx1296.

D. B. Mott, A. Waczynski, Y. Wen, W. Xia-Serafino, B. J. Rauscher, R. J. Hill, G. Delo, R. Foltz, E. Kan, M. P. Chiao, O. Fox, C. Cabelli, J. Garnett, M. Loose, S. Wong-Anglin, M. Zandian, D. Alexander, C. K. Brambora, R. Derro, T. Ellis, M. B. Garrison, B. Howe, T. E. Johnson, M. Jurado, S. S. Manthripragada, J. M. Marsh, C. Marshall, R. J. Martineau, J. Nieznanski, K. Novo-Gradac, W. D. Roher, M. T. Smith, D. Wilson, and P. Wallis. Characterization of the detector subsystem for near-infrared spectrograph (NIRSpec) on the James Webb Space Telescope. page 66900L, 9 2007. doi: 10.1117/12.734579.

J.-L. Puget, A. Abergel, J.-P. Bernard, F. Boulanger, W. B. Burton, F.-X. Desert, and D. Hartmann. Tentative detection of a cosmic far-infrared background with COBE. *Astronomy and Astrophysics*, 308:L5, Apr. 1996.

B. J. Rauscher, D. J. Lindler, D. B. Mott, Y. Wen, P. Ferruit, and M. Sirianni. The Dark Current and Hot Pixel Percentage of the James Webb Space Telescope 5μm Cutoff HgCdTe Detector Arrays as Functions of Temperature. *Publications of the Astronomical Society of the Pacific*, 123(906):953–957, 8 2011. ISSN 00046280. doi: 10.1086/661663.

B. E. Robertson, R. S. Ellis, S. R. Furlanetto, and J. S. Dunlop. Cosmic Reionization and Early Star-Forming Galaxies: A Joint Analysis of New Constraints from Planck and Hubble Space Telescope. 2 2015. doi: 10.1088/2041-8205/802/2/L19.

B. P. Schmidt. Nobel Lecture: Accelerating expansion of the Universe through observations of distant supernovae . *Reviews of Modern Physics*, 84(July):1151:1163, 2012. doi: 10.1103/RevModPhys.84.1151. URL https://journals.aps.org/rmp/pdf/10.1103/RevModPhys.84.1151.

H. Spinrad and R. P. S. Stone. An upper limit to the extragalactic background light. *The Astrophysical Journal*, 226:609, 12 1978. ISSN 0004-637X. doi: 10.1086/156645.

Teledyne. Teledyne Imaging Sensors HAWAII-2RG Visible and Infrared Focal Plane Array. URL http://www.oir.caltech.edu.

M. Trenti. Sky hopping with Australia's first space telescope - Pursuit: by The University of Melbourne, 2018a. URL https://pursuit.unimelb.edu.au/articles/sky-hopping-with-australia-s-first-space-telescope.

M. Trenti. Funding awarded for development of SkyHopper's innovative camera âĂŞ SkyHopper, 2018b. URL https://skyhopper.research.unimelb.edu.au/2018/05/01/funding-awarded-for-development-of-skyhoppers-innovative-camera/.

M. Trenti, L. D. Bradley, M. Stiavelli, P. Oesch, T. Treu, R. J. Bouwens, J. M. Shull, J. W. MacKenty, C. M. Carollo, and G. D. Illingworth. The brightest of reionizing galaxies survey: Design and preliminary results. *The Astrophysical Journal*, 727(2):L39, 1 2011. doi: 10.1088/2041-8205/727/2/l39.

K. Tsumura, J. Battle, J. Bock, A. Cooray, V. Hristov, B. Keating, D. H. Lee, L. R. Levenson, P. Mason, T. Matsumoto, S. Matsuura, U. W. Nam, T. Renbarger, I. Sullivan, K. Suzuki, T. Wada, and M. Zemcov. Observations of the near-infrared spectrum of the Zodiacal light with CIBER. *The Astrophysical Journal*, 719(1):394–402, 8 2010. ISSN 0004-637X. doi: 10.1088/0004-637X/719/1/394.

M. Zemcov, T. Arai, J. Battle, J. J. Bock, A. Cooray, V. Hristov, B. Keating, M.-G. Kim, D.-H. Lee, L. Levenson, P. Mason, T. Matsumoto, S. Matsuura, K. Mitchell-Wynne, U. W. Nam, T. Renbarger, J. Smidt, I. Sullivan, K. Tsumura, and T. Wada. Measuring Light from the Epoch of Reionization with CIBER, the Cosmic Infrared Background Experiment. 1 2011.

M. Zemcov, T. Arai, J. Battle, J. Bock, A. Cooray, V. Hristov, B. Keating, M. G. Kim, D. H. Lee, L. R. Levenson, P. Mason, T. Matsumoto, S. Matsuura, U. W. Nam, T. Renbarger, I. Sullivan, K. Suzuki, K. Tsumura, and T. Wada. The cosmic infrared background experiment (ciber): A sounding rocket payload to study the near infrared extragalactic background light. 207(2):31, 8 2013. doi: 10.1088/0067-0049/207/2/31.

M. Zemcov, J. Smidt, T. Arai, J. Bock, A. Cooray, Y. Gong, M. G. Kim, P. Korngut, A. Lam, D. H. Lee, T. Matsumoto, S. Matsuura, U. W. Nam, G. Roudier, K. Tsumura, and T. Wada. On the origin of near-infrared extragalactic background light anisotropy. *Science*, 346 (6210):732–735, 11 2014. ISSN 10959203. doi: 10.1126/science.1258168.

M. Zemcov, P. Immel, C. Nguyen, A. Cooray, C. M. Lisse, and A. R. Poppe. Measurement of the cosmic optical background using the long range reconnaissance imager on New Horizons. *Nature communications*, 8:15003, 2017. ISSN 2041-1723. doi: 10.1038/ncomms15003.